



Sn isotope fractionation during volatilization of Sn(IV) chloride: Laboratory experiments and quantum mechanical calculations

Jia-Xin She¹, Tianhua Wang¹, Hengdi Liang, M.N. Muhtar, Weiqiang Li^{*}
Xiandong Liu^{*}

State Key Laboratory for Mineral Deposits Research, School of Earth Sciences and Engineering, Nanjing University, Nanjing, Jiangsu 210023, PR China

Received 15 April 2019; accepted in revised form 23 October 2019; Available online 2 November 2019

Abstract

Volatilization is an important pathway of element transport in nature, and this process may be associated with stable isotope fractionation, which could be used to understand the elemental volatilization mechanisms. In this study, we report that evaporation of Sn(IV) chloride solution under experimental conditions (96 °C, 1 atmospheric pressure) results in significant loss of aqueous Sn(IV) and Sn stable isotope fractionation. The $\delta^{122/116}\text{Sn}$ of the residue solution can increase by up to 0.50‰ (or a 0.33‰ increase in $\delta^{122/118}\text{Sn}$) after repeated evaporation, indicating preferential partitioning of isotopically light Sn species into the vapor phase during evaporation. The observed Sn loss and associated Sn isotope fractionation during the evaporation experiments can be described using a Rayleigh fractionation function, with a best-fitting isotope fractionation factor of -0.36‰ in $\Delta^{122/116}\text{Sn}_{\text{vapor-aq}}$ (or -0.24‰ in $\Delta^{122/118}\text{Sn}_{\text{vapor-aq}}$). We also performed quantum mechanical calculations to assess the stability of different potential Sn(IV) species in aqueous and vapor phases, and derived the equilibrium Sn isotope fractionation factors between these Sn(IV) species. The calculation results suggest that the dominant gaseous species of Sn(IV), SnCl_4 , is isotopically heavier than the aqueous Sn(IV) species by 1.24‰–0.35‰ in $\delta^{122/116}\text{Sn}$ (or 0.82‰–0.19‰ in $\delta^{122/118}\text{Sn}$) under equilibrium at 96 °C, which is opposite to the experimental results. Such contrast in the direction of Sn isotope fractionation implies that kinetic isotope fractionation, rather than thermodynamic equilibrium isotope fractionation, took place for SnCl_4 in the evaporation experiments at 96 °C. The observed experimental data can be explained by a kinetic isotope fractionation model involving backward reaction of SnCl_4 vaporization at the solution-vapor boundary. This study, in combination with a recent report of positive $\Delta^{122/116}\text{Sn}_{\text{vapor-aq}}$ (or $\Delta^{122/118}\text{Sn}_{\text{vapor-aq}}$) factor during evaporation of SnCl_4 at 150 °C (Wang et al., 2019a), suggests that Sn(IV) volatilization mechanisms may be different with and without fluid boiling. Combined laboratory experiments and quantum mechanical calculations on the isotopic effects of Sn(IV) chloride solution evaporation provide important constraints for understanding the rapidly accumulating Sn isotopes data from studies on Sn ore-forming processes, bronze metallurgy and archeology, and volatile elements in planetary processes.

© 2019 Elsevier Ltd. All rights reserved.

Keywords: Evaporation; Sn isotope; Isotope fractionation; Quantum mechanical calculation

1. INTRODUCTION

^{*} Corresponding authors.

E-mail addresses: liweiqiang@nju.edu.cn (W. Li),
xiandongliu@gmail.com (X. Liu).

¹ The two authors contributed equally to this work.

Transport of metals as volatile species is ubiquitous in nature and it plays an important role in many processes.

<https://doi.org/10.1016/j.gca.2019.10.033>

0016-7037/© 2019 Elsevier Ltd. All rights reserved.

For example, huge amounts of metals (e.g., Cd, Hg) are released into atmosphere as gaseous species in a range of natural and anthropogenic processes, which contribute to the global cycling of these elements and have profound ecological and environmental consequences (Navarro-Flores et al., 2000; Tchounwou et al., 2003; Cloquet et al., 2006; Abascal et al., 2016). Brine-vapor separation has been suggested as a mechanism to enrich certain metals (i.e., Au, Cu, Sn) in different types of ore deposits (Heinrich et al., 1999), and transport of these metals in vapors leads to formation of magmatic-hydrothermal ore deposits (Williams-Jones and Heinrich, 2005; Pokrovski et al., 2013). Significant amounts of Au, Mo, and Cu are found in vapor phases based on fluid inclusions studies of porphyry deposits (Ulrich et al., 1999; Richards, 2011; Migdisov et al., 2014), and experiments show that the solubility of these metals in vapor are higher than those predicted based on conventional thermodynamic models (Williams-Jones et al., 2002). Condensates of volcanic vapors derived from active andesitic magmatism are commonly characterized by high contents of Cu, Zn, Pb, As, Mo, and Hg (Symonds et al., 1987; Chaplygin et al., 2016). Sn and Mo are also reported to occur in high concentrations in condensates of vapors released from rhyolitic and dacitic volcanoes (Giggenbach and Matsuo, 1991; Hedenquist et al., 1994; Chiaradia et al., 2018).

In addition to elemental transport, volatilization may contribute to isotopic variations of elements in nature (Richter et al., 2002; Xiao et al., 2007; Wang et al., 2012). Classic examples are H and O isotope fractionations during evaporation of water (Cappa et al., 2003; Luz et al., 2009; Gonfiantini et al., 2018). Evaporation of brines is also associated with Cl isotope fractionation (Rodríguez et al., 2018). Additionally, volatilization of some heavy metals (e.g., Cd and Hg) are accompanied with remarkable mass-dependent or mass-independent isotope fractionations (Wombacher et al., 2004; Cloquet et al., 2006; Estrade et al., 2009) on Earth. Furthermore, vaporization is an important planetary process that has been demonstrated to induce isotope fractionation of a wide range of elements including Ti (Zhang et al., 2014), K (Yu et al., 2003; Chen et al., 2019), Sn (Creech and Moynier, 2019; Wang et al., 2019b), Zn (Day et al., 2017; Pringle et al., 2017), Cr (Sossi et al., 2018), Cu (Moynier et al., 2010) and Mg (Richter et al., 2007). The isotopic fractionation between different phases reflects the geochemical and thermodynamic history of natural materials (Wunder et al., 2011), and fractionation of isotopes may be used to understand the volatilization processes.

In this study, we focus on the volatilization behavior of Sn(IV) chlorides and the associated isotopic effects. Tin is an important metal that is widely used in alloys, tin plating, solder, and optoelectronics, as well as ancient bronzes. Tin is tetravalent in cassiterite, and probably also exists in tetravalent forms in granitic melts (Heinrich, 1990). Tin in magmatic fluids predominantly occurs as Sn-Cl complexes, including fluorite- or topaz-saturated magmatic systems (Heinrich, 1990). In mineralization processes, Sn occurs as Sn(II) and Sn(IV) chloride complexes in hydrothermal fluids (Bruger et al., 2016; Schmidt, 2018). Transport of Sn

by vapor has been reported from hydrothermal and magmatic systems (Giggenbach and Matsuo, 1991; Heinrich et al., 1999; Chiaradia et al., 2018). In planetary processes, Sn behaves as a moderate volatile element with a 50% condensation temperature of 704 K (Lodders, 2003) and is depleted in the inner solar system (Anders and Ebihara, 1982; Holland and Turekian, 2003; Righter et al., 2018).

Tin has ten stable isotopes with atomic mass number ranging from 112 to 124. Stable isotopes of Sn have been employed to study planetary processes (Delaeter and Jeffery, 1967; Delaeter et al., 1974; Loss et al., 1990; Creech and Moynier, 2019), magmatic processes (Badullovich et al., 2017; Wang et al., 2018), and hydrothermal mineralization processes (Yao et al., 2018). Only a few studies have investigated Sn isotope fractionation by experiments. For example, Malinovskiy et al. (2009) reported that photolysis of methyl tin results in preferential release of light isotopes of Sn. Mathur et al. (2017) noticed that Sn can be volatilized by HI with significant Sn isotope fractionation. More recently, Wang et al. (2019a) experimentally showed that a variety of processes, including evaporation of Sn chlorides, can induce remarkable Sn isotope fractionation. Here we focus on the topic of evaporation of Sn(IV) chloride solutions and its isotopic effects without the impact of Sn redox processes. Compared to the Sn(IV) chloride evaporation experiment of Wang et al. (2019a), our experiments were systematically conducted at a lower temperature with a wider range of solution matrix, allowing better constraints of the Sn isotope fractionation behavior. We compare the observed experimental results with stability data and inter-species Sn isotope fractionation obtained by quantum mechanical calculation to shed insights into the mechanistic details of Sn volatilization and isotope fractionation behaviors, and further discuss the implications.

2. EXPERIMENTAL

2.1. Evaporation experiments

Double distilled hydrochloric acid, nitric acid, and deionized (18.2 MΩ/cm) water were used in all experiments. Teflon beakers, centrifuge tubes and pipette tips were soaked in 6 M HCl overnight and then rinsed with deionized water before usage. Earlier evaporation experiments used a 1000 µg/mL pure Sn elemental standard solution from SPEX CertiPrep. After exhaustion of the SPEX Sn elemental standard solution, a 1000 µg/mL Sn stock solution was prepared by dissolving analytical grade SnCl₄·5H₂O salt in 2 M HCl. A 2 M HCl matrix was used to prevent Sn loss by precipitation of hydrolysis products of Sn (Delaeter et al., 1974; Yi et al., 1995). A 30-mL Sn stock solution was mixed with 1–2 mL sodium standard solution (10000 µg/mL, SPEX CertiPrep) and 2–4 mL cobalt standard solution (1000 µg/mL, SPEX CertiPrep) to make a stock solution for evaporation experiments. Sodium and cobalt were used as two independent internal elemental standards for monitoring the degree of Sn loss during evaporation.

Evaporation experiments were performed on a hotplate heating at a constant temperature of 96 °C in a laminar flow hood (Class-100) in a clean room (Class-1000) with filtered air at State Key Laboratory for Mineral Deposits Research, Nanjing University. For each experiment, 1 mL of the stock solution was evaporated to dryness in a 7 mL Teflon beaker over 12 hours, and then 1 mL of HCl with a varying molarity was added to the beaker and heated again to dryness. The molarity of HCl varied (0.5 M, 1 M, 2 M, 3 M, and 4 M) in different sets of evaporation experiments. In each set of evaporation experiment, parallel samples were treated, and the samples were dissolved in HCl and evaporated to dryness by different times ($n = 1$ to 5) prior to sampling (see appendix Fig. S1). After evaporation experiments, each of the sample was re-dissolved in 3 mL 2 M HCl, and 500 μ L of the dissolved sample was taken for elemental analysis and the remaining solution was used for isotopic analysis.

2.2. Elemental analysis

Elemental concentrations were analyzed using inductively coupled plasma optical emission spectrometry (ICP-OES) with a Skyray[®] ICP-3000 instrument. A 500 μ L fraction of the dissolved sample solution collected after evaporation experiments was diluted to 4 mL (8 times dilution) with 2 M HCl and analyzed for Sn, Na and Co concentrations. A series of gravimetrically prepared multi-element standards were used for calibration and instrument drift correction. An independent standard solution was bracketed between five to ten samples to monitor the stability of the instrument. External precision of the elemental analysis was better than 10% (2 relative standard deviation).

2.3. Tin isotope analysis

Tin isotope analysis was performed using a Thermo Fisher Scientific Neptune Plus multi-collector inductively-coupled plasma mass spectrometer (MC-ICP-MS) at Nanjing University. The instrument was running at low mass resolution and wet-plasma mode, using a 100 μ L/min self-aspirating nebulizer tip and a glass spray chamber (Du et al., 2017). A combined standard-sample-standard bracketing and external correction method (Marechal et al., 1999; Li et al., 2009) was applied for Sn isotope measurements. Based on the elemental concentration analytical results, an aliquot of the dissolve samples that contained 5 μ g of Sn was diluted to 1 ± 0.1 ppm (5 mL) to match the concentration of an in-house standard, and the sample and standard solutions were both doped with 0.3 ppm Sb (SPEX CertiPrep) for external mass bias correction using $^{123/121}\text{Sb}$ ratios and the exponential mass fractionation law. A 40 s on-peak acid blank was measured before each analysis and each Sn isotope ratio measurement comprised fifty 4-s integrations. Two Sn isotope standards have been used for reporting Sn isotope data in recent literature, including the Sn_IPGP standard (Badullovich et al., 2017; Creech et al., 2017; Creech and Moynier, 2019) and NIST SRM 3161a (Mathur et al., 2017; Wang et al., 2017; Yao

et al., 2018; Wang et al., 2019a, 2019b). During the Sn isotope analyses in this study, NIST SRM 3161a (Lot #140917) was used as the bracketing standard, and isotope data was reported primarily in delta notation ($\delta^{122/116}\text{Sn}$) relative to the reference standard NIST SRM 3161a:

$$\delta^{122/116}\text{Sn} (\text{‰}) = \left[\left(\frac{^{122}\text{Sn}/^{116}\text{Sn}}{^{122}\text{Sn}/^{116}\text{Sn}} \right)_{\text{sample}} / \left(\frac{^{122}\text{Sn}/^{116}\text{Sn}}{^{122}\text{Sn}/^{116}\text{Sn}} \right)_{3161a} - 1 \right] \times 1000$$

Repeat measurements for multiple Sn solution standards over long-term were made for the estimation of external analytical precision (Fig. 1a). Mean Sn isotope compositions of Spex CertiPrep Sn, NIST SRM 3161a, and an in-house solution of SnCl₄ are $0.38 \pm 0.07\text{‰}$ ($n = 66$, 2SD), $-0.01 \pm 0.06\text{‰}$ ($n = 76$, 2SD), and $0.18 \pm 0.09\text{‰}$ ($n = 58$, 2SD), respectively. $\delta^{122/118}\text{Sn}$ value were also presented for comparison and further use (Table 2 and Table S3). Typical internal precision for $^{122}\text{Sn}/^{116}\text{Sn}$ ratio analysis is better than $\pm 0.04\text{‰}$, and the long-term external reproducibility of $\delta^{122/116}\text{Sn}$ analysis is constrained to be better than $\pm 0.09\text{‰}$.

For the purpose of interlaboratory comparison, we also calibrated the Sn isotope composition of Sn_IPGP, which has a $\delta^{122/116}\text{Sn}$ value of $0.27 \pm 0.09\text{‰}$ ($\delta^{122/118}\text{Sn} = 0.17 \pm 0.06\text{‰}$) ($n = 35$, 2SD) relative to NIST SRM 3161a (Lot #140917). Therefore, all Sn isotope data are also reported in delta notation ($\delta^{122/118}\text{Sn}$) relative to Sn_IPGP standard following the convention of the IPGP research group:

$$\delta^{122/118}\text{Sn} (\text{‰}) = \left[\left(\frac{^{122}\text{Sn}/^{118}\text{Sn}}{^{122}\text{Sn}/^{118}\text{Sn}} \right)_{\text{sample}} / \left(\frac{^{122}\text{Sn}/^{118}\text{Sn}}{^{122}\text{Sn}/^{118}\text{Sn}} \right)_{\text{IPGP}} - 1 \right] \times 1000$$

NIST SRM 3161a (Lot #140917) has a $\delta^{122/118}\text{Sn}$ value of -0.17‰ relative to Sn_IPGP (Fig. 1b).

2.4. Matrix effect

Natural samples could have complex matrix compositions and the matrix effect needs to be assessed to assure accurate and precise isotope results. Investigations concerning matrix effects of Sn isotope measurements have been reported in Schulze et al. (2017) and references therein. In this study, we doped the standard Sn (NIST 3161a) solution with variable amounts of Ba, Ca, Cu, Fe, Na, and Si and analyzed the doped standard solutions as unknowns. The ratios of matrix elements to Sn were 1:1, 3:1, 10:1, and 30:1. The doping experiments show that when the $[\text{M}]/[\text{Sn}]$ ratio (mass/mass) is as low, the measurement of $\delta^{122/116}\text{Sn}$ is not significantly affected by matrix element considering an external analytical uncertainty of $\pm 0.09\text{‰}$ (or $\pm 0.06\text{‰}$ in $\delta^{122/118}\text{Sn}$), regardless of the mass and chemical property of the doped matrix element (Fig. 2a, b; Table S6). For the evaporation experiments, the analyzed Sn solutions contained Na and Co with a $[\text{M}]/[\text{Sn}]$ ratio of less than 2.74 (Table 2). Therefore, the measured $\delta^{122/116}\text{Sn}$ values for the Sn solutions after the evaporation experiments were precise and accurate to a level of better than $\pm 0.09\text{‰}$ (or $< \pm 0.06\text{‰}$ in $\delta^{122/118}\text{Sn}$), the external precision.

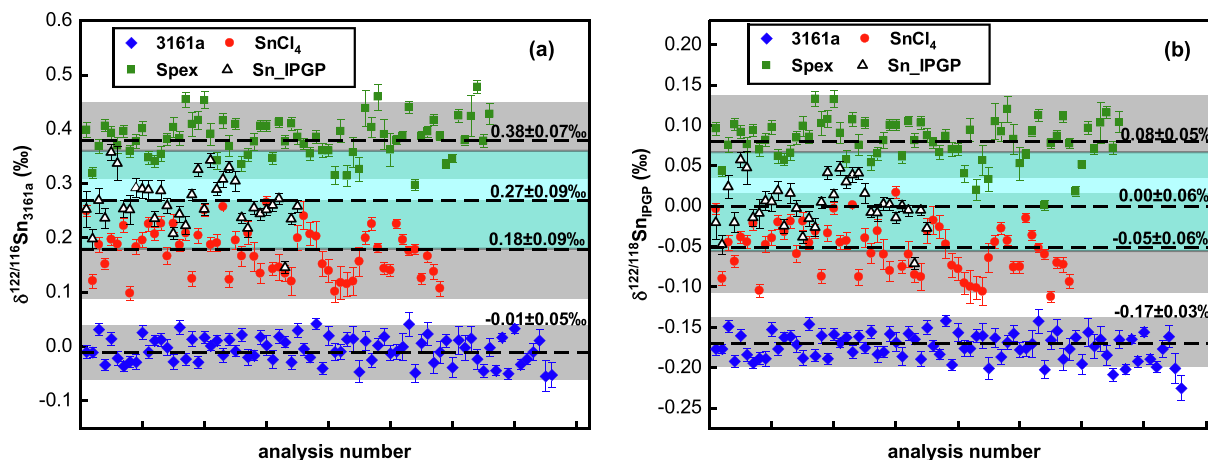


Fig. 1. Long-term reproducibility of Sn isotope standards over 2 years: (a) $\delta^{122/116}\text{Sn}$ values relative to 3161a standard; (b) $\delta^{122/118}\text{Sn}$ values relative to Sn_IPGP standard. Error bars represent two standard error (internal precision) for individual analysis. Shaded areas represent 2SD of multiple analyses.

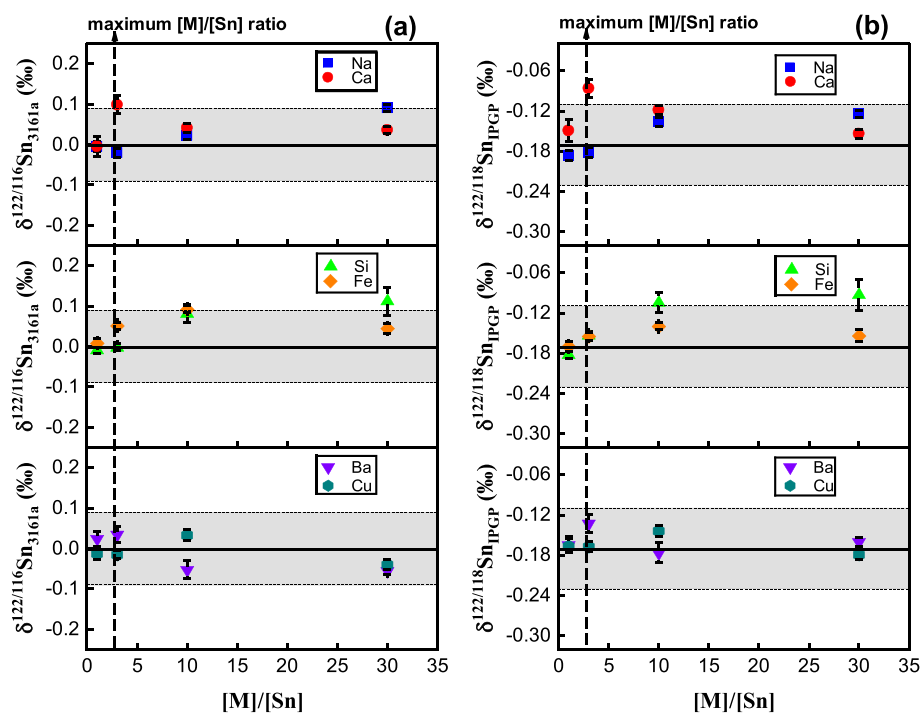


Fig. 2. Plots of matrix element doping experiments to verify the robustness of Sn isotope analytical method against matrix elements, shaded area represents the external uncertainty of Sn isotope analysis, dash line ($[\text{M}]/[\text{Sn}] = 2.74$) denotes the maximum matrix-to-Sn ratio for Sn solutions that were analyzed in this study. (a) $\delta^{122/116}\text{Sn}$ values relative to 3161a standard; (b) $\delta^{122/118}\text{Sn}$ values relative to Sn_IPGP standard.

3. THEORETICAL CALCULATIONS

Parallel to experiments, we performed first principles molecular dynamics (FPMD) simulations and static quantum mechanical calculations to constrain the stabilities of possible species of Sn in aqueous and vapor phases. Based on these results, we calculated the equilibrium Sn isotope fractionation factors between the stable Sn(IV) species using static quantum mechanical calculations.

3.1. First principles molecular dynamics

3.1.1. Model setup

SnCl_6^{2-} , $\text{SnCl}_5(\text{H}_2\text{O})^-$ and $\text{SnCl}_4(\text{H}_2\text{O})_2$ have been proposed as the stable species for Sn(IV) in aqueous solution in previous studies (Sherman et al., 2000; Schmidt, 2018). There are two isomers of $\text{SnCl}_4(\text{H}_2\text{O})_2$. The *cis*- isomer of $\text{SnCl}_4(\text{H}_2\text{O})_2$ has two H_2O ligands next to each other (i.e., O-Sn-O has an angle of about 90°), whereas in the *trans*-

isomer of $\text{SnCl}_4(\text{H}_2\text{O})_2$ the two H_2O ligands are at opposite positions of the molecule (i.e., O-Sn-O has an angle of about 180°). The structures of these aqueous species are shown in Fig. 5. The protonated forms such as $\text{SnCl}_5(\text{HCl})^-$ can hardly exist because of the extremely low pK_a of HCl (Perrin, 1982). In vapor phase, the charged species is not favored due to the low dielectric constant of the vapor (Pokrovski et al., 2013), so the possible vapor species of Sn(IV) considered in this study include SnCl_4 , $\text{SnCl}_4(\text{H}_2\text{O})$ and *cis- / trans*- $\text{SnCl}_4(\text{H}_2\text{O})_2$.

For modeling of aqueous solutions, we set the simulation cells as 3D periodic boundary cubic boxes with a side length of 12.43 Å. The simulated systems at 330 K and 368 K are listed in Table 1. The temperature of 330 K was set for the ambient conditions to avoid the glassy behavior of liquid water at lower temperatures (VandeVondele et al., 2005b). For pure water system, the number of water molecules in the simulation box is calculated from the density of liquid water under each temperature and the corresponding saturated vapor pressure (P_{sat}) estimated with the equation of state of water (Wagner et al., 2000). We replaced one H_2O molecule with one Cl^- ion, deriving the numbers of solvent water molecules listed in Table 1. This approach has been proven reasonable and used in previous FPMD studies of aqueous solutions (Sulpizi and Sprik, 2008; Liu et al., 2012). For simulations of vapor phases, cubic boxes with a side length of 15.00 Å were used. The initial models of SnCl_4 , $\text{SnCl}_4(\text{H}_2\text{O})$ and *cis- / trans*- $\text{SnCl}_4(\text{H}_2\text{O})_2$ were placed at the center of the boxes without any water molecule. The simulations were carried out at 300 K and 368 K, respectively.

3.1.2. Computational details

FPMD simulations were carried out using a CP2K/QUICKSTEP package (VandeVondele et al., 2005a). In this code, density functional theory (DFT) was implemented based on the mixed Gaussian and plane waves approach (GPW) (Lippert et al., 1997). DZVP (double-zeta valence polarizable) basis sets (VandeVondele and Hutter, 2007), PBE (Perdew-Burke-Ernzerhof) exchange-correlation functional (Perdew et al., 1996) and GTH (Goedecker-Teter-Hutter) pseudopotentials (Goedecker et al., 1996) were employed. The electron density cutoff was set to be 280 Ry. Comparisons with a higher cutoff of 600 Ry prove that 280 Ry is reasonable for these systems (see the Appendix, comparisons between cutoff 280 Ry and 600 Ry). The simulations were performed in canonical (NVT) ensemble and the temperatures were controlled with the Nosé-Hoover chain thermostat (Hoover, 1985; Nose, 1984a, b). Each simulation was performed with a time step

of 0.5 fs. After a pre-equilibration for at least 5.0 ps, the production run for over 25.0 ps was performed.

3.2. Static quantum mechanical calculations

3.2.1. Free energy calculations

To determine the relative stabilities of SnCl_4 , $\text{SnCl}_4(\text{H}_2\text{O})$ and *cis- / trans*- $\text{SnCl}_4(\text{H}_2\text{O})_2$ in vapor phases, the Gibbs free energy changes (ΔG) of the dehydration processes (from *cis- / trans*- $\text{SnCl}_4(\text{H}_2\text{O})_2$ to SnCl_4 , reactions in Table 4) were investigated by using static quantum mechanical calculations:

$$\Delta G = \sum G_{\text{prod}} - \sum G_{\text{react}} \quad (1)$$

where $\sum G_{\text{prod}}$ and $\sum G_{\text{react}}$ are the total Gibbs free energy values of products and reactants, respectively. The Gibbs free energy is defined as

$$G = H - TS \quad (2)$$

where H, T and S are the enthalpy, temperature and entropy, respectively. The enthalpy and entropy can be decomposed into several terms:

$$H = E_0 + E_{\text{elec}} + E_{\text{trans}} + E_{\text{rot}} + E_{\text{vib}} + k_B T \quad (3)$$

$$S = S_{\text{elec}} + S_{\text{trans}} + S_{\text{rot}} + S_{\text{vib}} \quad (4)$$

where E_0 is total electronic energy. E_{elec} , E_{trans} , E_{rot} and E_{vib} are internal energy of electronic motion, translation, rotational motion and vibrational motion, respectively. S_{elec} , S_{trans} , S_{rot} and S_{vib} are entropy of electronic motion, translation, rotational motion and vibrational motion, respectively. k_B is the Planck constant. The details for the calculations of those terms can be found in McQuarrie and Simon (1999). These quantities are provided in the output of Gaussian (Foresman and Frisch, 2015). The contribution of translational entropy ($-TS_{\text{trans}}$) is calculated with

$$-TS_{\text{trans}} = -RT \left(\ln \left(\left(\frac{2\pi m k_B T}{h^2} \right)^{\frac{3}{2}} \cdot \frac{k_B T}{P_0} \right) + \frac{5}{2} \right) \quad (5)$$

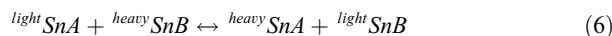
where P_0 is the pressure of reference state (1 atm in Gaussian). For water, a term of $RT \ln \left(\frac{P_{\text{sat}}}{P_0} \right)$ is added to convert it to the value under the saturated vapor pressure (P_{sat}) at T. This term is equal to -2.1 kcal/mol at 298.15 K, -0.1 kcal/mol at 368 K and 1.3 kcal/mol at 423 K, respectively.

3.2.2. Thermodynamic equilibrium isotope fractionation

For thermodynamic equilibrium isotope fractionation, we consider the exchange between two tin isotopomers:

Table 1
Parameters of the simulation cells for first principle molecular dynamics calculation for aqueous phases of Sn(IV) chlorides.

Temperature	Complex	Number of water molecules
330 K	SnCl_6^{2-}	58
	$\text{SnCl}_5(\text{H}_2\text{O})^-$	58
	<i>cis- / trans</i> - $\text{SnCl}_4(\text{H}_2\text{O})_2$	58
	SnCl_6^{2-}	56
368 K	$\text{SnCl}_5(\text{H}_2\text{O})^-$	56
	<i>cis- / trans</i> - $\text{SnCl}_4(\text{H}_2\text{O})_2$	56



where light Sn and heavy Sn represent the light and heavy isotopes of Sn, respectively. The Sn isotope fractionation factor ($\alpha_{\text{SnA-SnB}}$) between SnA and SnB can be expressed as

$$\alpha_{\text{SnA-SnB}} = \left(\frac{\text{heavy Sn}}{\text{light Sn}} \right)_{\text{SnA}} / \left(\frac{\text{heavy Sn}}{\text{light Sn}} \right)_{\text{SnB}} = \frac{\beta_{\text{SnA}}}{\beta_{\text{SnB}}} \quad (7)$$

where β_{SnA} and β_{SnB} are the reduced partition function ratio (RPF) of Sn isotopes in SnA and SnB , respectively, and $\Delta_{\text{SnA-SnB}}$, the difference in measured Sn isotope compositions between SnA and SnB , can be defined as:

$$\Delta_{\text{SnA-SnB}} \approx 1000 \ln \alpha_{\text{SnA-SnB}} = 1000 \ln \beta_{\text{SnA}} - 1000 \ln \beta_{\text{SnB}} \quad (8)$$

According to Urey (1947) and Bigeleisen and Mayer (1947), the β factor or RPF can be approximated using the harmonic vibrational frequencies of isotopomer,

$$\beta_{\text{SnA}} = \text{RPF}_{\text{SnA}} = \prod_{i=1}^{3n-6} \frac{\text{heavy } u_i}{\text{light } u_i} \cdot \frac{e^{-\frac{\text{heavy } u_i}{2}}}{1 - e^{-\text{heavy } u_i}} \cdot \frac{1 - e^{-\frac{\text{light } u_i}{2}}}{e^{-\frac{\text{light } u_i}{2}}} \quad (9)$$

with

$$u_i = \frac{h\nu_i}{k_B T} \quad (10)$$

where $3n-6$ is the number of harmonic vibrational modes of non-linear isotopomer containing n atoms; h , ν_i , k_B and T are the Planck constant, vibrational frequency, Boltzmann constant and temperature, respectively. For SnB we have the same formula.

3.2.3. Computational details

The harmonic vibrational frequencies of molecules can be efficiently obtained through quantum chemistry calculation, allowing derivation of some thermodynamic quantities and the equilibrium fractionation factor between different species. Quantum chemistry calculations have been widely used to calculate the equilibrium fractionation factors in the systems of geological interest (Schauble, 2004; Blanchard et al., 2017). In this study, we focus on the fractionation of ^{122}Sn and ^{116}Sn or ^{118}Sn isotopes among the stable $\text{Sn}^{4+}-\text{Cl}^-$ species derived from FPMD simulations. For the aqueous species, SnCl_6^{2-} , $\text{SnCl}_5(\text{H}_2\text{O})^-$ and *cis*-/*trans*- $\text{SnCl}_4(\text{H}_2\text{O})_2$ were investigated with 18 solvent water molecules accounting for the solvation effect. We also calculated SnCl_6^{2-} and *cis*- $\text{SnCl}_4(\text{H}_2\text{O})_2$ with 24 solvent water molecules, but found no obvious difference, indicating that 18 water molecules are sufficient (Appendix Table S1). DFT calculations were carried out using a Gaussian 09 package (Frisch et al., 2013). B3LYP hybrid exchange–correlation functional (Lee et al., 1988; Becke, 1993) was used with def2-TZVP basis sets (Weigend and Ahlrichs, 2005).

4. RESULTS

4.1. Elemental behaviors during evaporation

After repeated evaporation, the two reference elements (Na and Co) maintained a constant ratio within analytical uncertainty (Table S2) for each evaporation series (Fig. 3a, b), suggesting that both elements were retained in the bea-

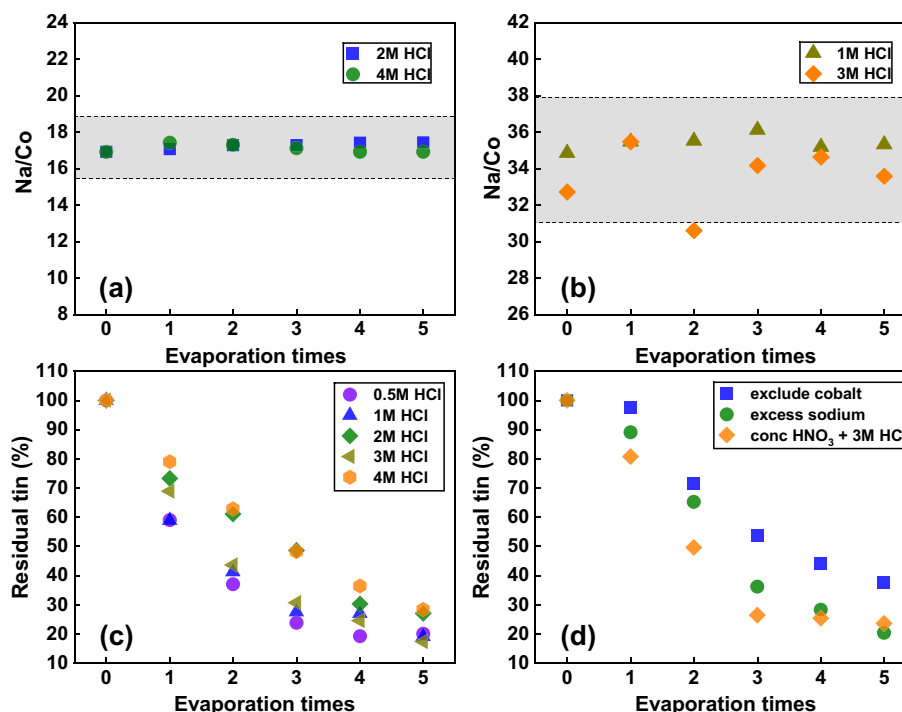


Fig. 3. (a) The optical emission light intensity ratio of Na to Co measured by ICP-OES for the evaporation series for 2 M and 4 M HCl; (b) The optical emission light intensity ratio of Na to Co measured by ICP-OES for the evaporation series for 1 M and 3 M HCl; (c) The fraction of residual Sn versus evaporation times in HCl of different molarities; (d) Control experiments showing the Sn loss versus evaporation times in different acid matrix or under different reference element concentrations.

Table 2
Tin isotope compositions of samples from evaporation experiments in this study.

Evaporation times	Concentration of HCl	F _{remaining}	$\delta^{122/116}\text{Sn}_{3161a}$ (‰)	$\delta^{122/118}\text{Sn}_{3161a}$ (‰)	$\delta^{122/116}\text{Sn}_{\text{IPGP}}$ (‰)	$\delta^{122/118}\text{Sn}_{\text{IPGP}}$ (‰)	$\Delta^{122/116}\text{Sn}$ (‰)	2SD (‰)	$\Delta^{122/118}\text{Sn}$ (‰)	2SD (‰)	Na/Sn (ppm/ppm)	Co/Sn (ppm/ppm)	Analysis number
0		1	0.45	0.29	0.18	0.12					0.62	0.11	n = 1
1	2 N	0.73	0.60	0.38	0.33	0.21	0.15	0.12	0.09	0.09	0.85	0.15	n = 1
2	2 N	0.61	0.74	0.47	0.47	0.3	0.29	0.12	0.18	0.09	1.04	0.18	n = 1
3	2 N	0.49	0.79	0.49	0.52	0.32	0.34	0.12	0.2	0.09	1.31	0.23	n = 1
4	2 N	0.30	0.94	0.62	0.67	0.45	0.49	0.12	0.33	0.09	2.13	0.38	n = 1
5	2 N	0.27	0.88	0.57	0.61	0.4	0.43	0.12	0.28	0.09	2.40	0.42	n = 1
1	4 N	0.79	0.55	0.36	0.28	0.19	0.10	0.12	0.07	0.09	0.81	0.14	n = 1
2	4 N	0.63	0.72	0.46	0.45	0.29	0.27	0.12	0.17	0.09	1.01	0.18	n = 1
3	4 N	0.48	0.63	0.41	0.36	0.24	0.18	0.12	0.12	0.09	1.30	0.23	n = 1
4	4 N	0.36	0.78	0.50	0.51	0.33	0.33	0.12	0.21	0.09	1.71	0.31	n = 1
5	4 N	0.28	0.95	0.62	0.68	0.45	0.50	0.12	0.33	0.09	2.21	0.40	n = 1
0		1	0.07	0.07	-0.2	-0.1					0.70	0.14	n = 2
1	1 N	0.59	0.25	0.19	-0.02	0.02	0.17	0.13	0.12	0.07	1.23	0.23	n = 2
2	1 N	0.41	0.34	0.26	0.07	0.09	0.28	0.10	0.19	0.06	1.77	0.34	n = 2
3	1 N	0.27	0.48	0.37	0.21	0.2	0.41	0.10	0.3	0.06	2.74	0.51	n = 2
0		1	0.08	0.05	-0.19	-0.12					0.66	0.14	n = 1
1	3 N	0.69	0.21	0.14	-0.06	-0.03	0.13	0.12	0.09	0.09	1.05	0.20	n = 1
2	3 N	0.43	0.33	0.22	0.06	0.05	0.25	0.12	0.17	0.09	1.44	0.32	n = 1

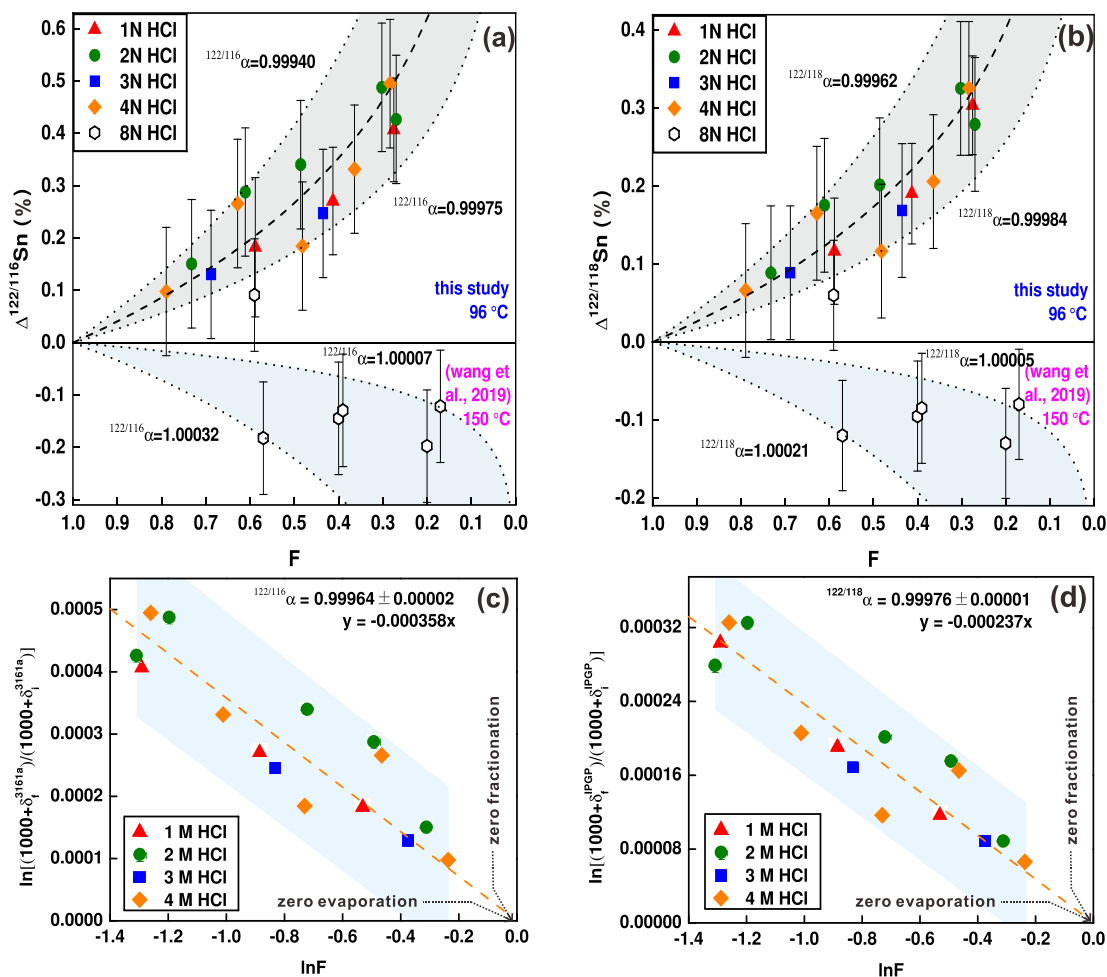


Fig. 4. (a) Plot of $\Delta^{122/116}\text{Sn}$; (b) Plot of $\Delta^{122/118}\text{Sn}$ versus F in linear space, the dotted lines represent the Rayleigh fractionation trends with different instantaneous fractionation factors α , defining a shade area that included all experimental data. The solid points are data from this study at 96 °C while the open points are data from Wang et al. (2019a) at 150 °C. (c) Plot of Sn isotope data ($\delta^{122/116}\text{Sn}$ values relative to 3161a standard); (d) Plot of Sn isotope data ($\delta^{122/118}\text{Sn}$ values relative to Sn_{IPGP} standard) versus F in logarithmic space. A least squares linear fitting was made in this plot give an estimate of instantaneous fractionation factors α .

ker and were not lost into vapor phases. We use Co as the reference to evaluate the variation of the Sn content before and after the evaporation experiments. The fraction of residual Sn relative to the original Sn content in the solution (F) is expressed as

$$F = \text{Sn}_{\text{final}}/\text{Sn}_{\text{initial}} = (\text{I}_{\text{Co}}/\text{I}_{\text{Sn}})_{\text{initial}}/(\text{I}_{\text{Co}}/\text{I}_{\text{Sn}})_{\text{final}}$$

where $(\text{I}_{\text{Co}}/\text{I}_{\text{Sn}})$ is the ratio of intensity for characteristic optical emission light wavelengths for Co (228.616 nm) and Sn (189.989 nm) measured by ICP-OES. Usage of Sn/Co ratio eliminates uncertainties in dissolution and dilution and leads to better constraints of the degree of Sn loss in the evaporation experiments. In the following discussion, the F factor is used to quantify the Sn loss by evaporation.

As shown in Fig. 3c, Sn was significantly lost from aqueous solution after evaporation (Table S2). Between 17% and 42% of Sn was lost in each round of evaporation, and after five times of evaporation, the mass of the residue Sn was mostly below 30% of the initial Sn. Control experiments show that Sn loss is not affected by the existence

of Co or Na in solution (Fig. 3d). Existence of HNO_3 in the HCl matrix does not prevent evaporative Sn loss, either (Fig. 3d), despite that HNO_3 can induce hydrolysis and precipitation of Sn (Haustein et al., 2010).

4.2. Isotope results for evaporation experiments

All measured isotope ratios of Sn in different samples follow mass dependent relations (appendix Fig. S2, Table S3). The $\delta^{122/116}\text{Sn}$ values for the residual samples for the evaporation experiments with 2 M and 4 M HCl vary from $0.95 \pm 0.09\text{‰}$ to $0.45 \pm 0.09\text{‰}$, whereas those for evaporation experiments with 1 M and 3 M HCl vary from $0.48 \pm 0.06\text{‰}$ to $0.07 \pm 0.09\text{‰}$ (Table 2). The different range in Sn isotope data for the experiments was caused by usage of different Sn solutions (SnCl_4 vs. Spex Sn) that have different initial values. For the convenience of discussion, we concentrate on the isotopic change in the residue material relative to the initial Sn solutions, or $\Delta^{122/116}\text{Sn}$ (‰) (Table 2). The Sn isotope fractionation factors for the evap-

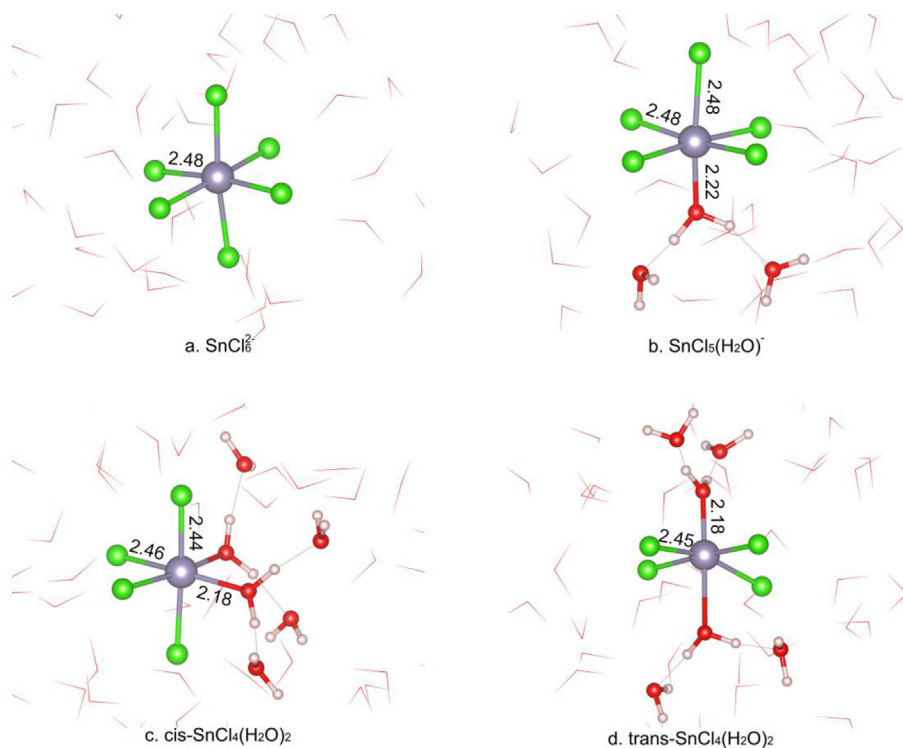


Fig. 5. Snapshots of SnCl_6^{2-} , $\text{SnCl}_5(\text{H}_2\text{O})^-$, *cis*- and *trans*- $\text{SnCl}_4(\text{H}_2\text{O})_2$ in aqueous solutions at 330 K. The average bond lengths in angstrom (\AA) are dimensioned therein. Sn = gray, Cl = green, O = red and H = pink. Some water molecules are removed for clarity.

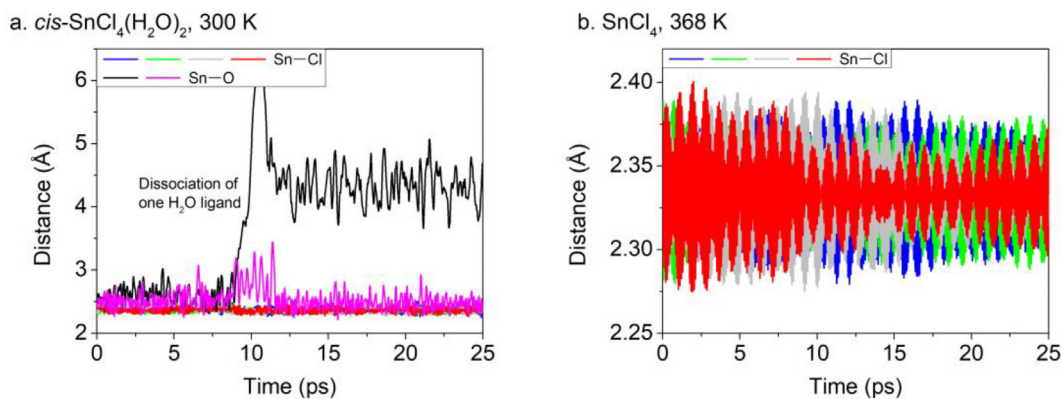


Fig. 6. Trajectories of Sn—Cl/ OH_2 distances in the simulation of *cis*- $\text{SnCl}_4(\text{H}_2\text{O})_2$ in vapor phase at 300 K (a) and Sn—Cl distances in the simulation of SnCl_4 at 368 K (b).

oration experiment sets range from 0.50‰ to 0.10‰ in $\Delta^{122/116}\text{Sn}$ (Fig. 4a), or 0.07‰ to 0.33‰ in $\Delta^{122/118}\text{Sn}$ (Fig. 4b).

Wang et al. (2019a) performed SnCl_4 evaporation experiments, in which SnCl_4 in 6 mL 8 M HCl on a Teflon dish was heated at 150 °C. Every time 0.1 mL solution was sampled at the time interval of 4 to 5 minutes. Wang et al. (2019a) reported their Sn isotope data in $^{124/116}\text{Sn}$, which are translated to $^{122/116}\text{Sn}$ or $^{122/118}\text{Sn}$ ratios based on mass dependent relations of stable isotope fractionation for comparison with our study. The observed $\Delta^{122/116}\text{Sn}$ for SnCl_4 solution during evaporation experiments of Wang et al. (2019a) ranged from -0.12‰ to -0.20‰ , with an exception

for the first data point, which is 0.09‰ (Fig. 4a); correspondingly, the $\Delta^{122/118}\text{Sn}$ values are 2/3 of the $\Delta^{122/116}\text{Sn}$ values (Fig. 4b), following a mass-dependent relation.

4.3. Computational results

4.3.1. First principles molecular dynamics

The FPMD simulations indicate that all of the four complexes stayed stable in aqueous solution in the period of simulation. There is no notable difference between the molecular structures for Sn species at 330 K and 368 K. The average Sn—Cl bond lengths of SnCl_6^{2-} , $\text{SnCl}_5(\text{H}_2\text{O})^-$, *cis*- and *trans*- $\text{SnCl}_4(\text{H}_2\text{O})_2$ in aqueous solutions are 2.48 \AA ,

Table 3
Bond length (Å) and vibrational frequencies (cm⁻¹) of SnCl₄.

Bond length ^a	Vibrational frequencies				Method
2.31	93.73	123.75	349.22	388.39	This study
2.315	94	124	367	409	CCSD(T) ^b
2.286	96.2	125.7	370.0	409.3	CCSD(T), MP2 ^c
2.29 / 2.30					Electron diffraction ^d
2.31					Electron diffraction ^e
2.28					Electron diffraction ^f
	95.2	126.1	369.1	408.2	Raman spectra ^g
		126.8		409.4	Infrared spectra ^h

^a See review in Hargittai (2000) for more calculated bond length values.

^b Kalugina and Thakkar (2015).

^c Thanthiriwatte et al. (2015). Structure is at the CCSD(T) level and frequencies are at the MP2 level.

^d Brockway and Wall (1934); Pauling and Brockway (1935).

^e Livingston and Rao (1959).

^f Fujii and Kimura (1970).

^g Clark and Rippon (1972); Clark and Mitchell (1975).

^h Koniger and Muller (1975).

Table 4
Gibbs free energy changes (ΔG) of the dehydration processes of SnCl₄(H₂O) and *cis*- / *trans*-SnCl₄(H₂O)₂ in vapor phase.

Reaction	T-P condition (K, bar)	ΔG (kcal/mol)
SnCl ₄ (H ₂ O) → SnCl ₄ + H ₂ O	298.15, 0.03 (P _{sat})	-6.3
	368, 0.84 (P _{sat})	-6.1
	423, 4.76 (P _{sat})	-6.1
<i>cis</i> -SnCl ₄ (H ₂ O) ₂ → SnCl ₄ (H ₂ O) + H ₂ O	298.15, 0.03	-7.3
	368, 0.84	-7.7
	423, 4.76	-8.1
<i>trans</i> -SnCl ₄ (H ₂ O) ₂ → SnCl ₄ (H ₂ O) + H ₂ O	298.15, 0.03	-13.7
	368, 0.84	-14.2
	423, 4.76	-14.7

Table 5
Calculated 1000ln^{122/116}β and 1000ln^{122/118}β values for the Sn⁴⁺-Cl⁻ species at ambient and elevated temperatures.

System	1000ln ^{122/116} β			1000ln ^{122/118} β		
	25 °C	96 °C	150 °C	25 °C	96 °C	150 °C
SnCl ₄	6.56	4.35	3.34	4.33	2.88	2.21
SnCl ₄ (H ₂ O)	6.16	4.09	3.13	4.07	2.70	2.07
SnCl ₆ ²⁻	4.65	3.05	2.33	3.07	2.02	1.54
SnCl ₅ (H ₂ O) ⁻	5.29	3.50	2.68	3.50	2.31	1.77
<i>cis</i> -SnCl ₄ (H ₂ O) ₂	5.89	3.90	2.99	3.89	2.58	1.98
<i>trans</i> -SnCl ₄ (H ₂ O) ₂	5.83	3.86	2.96	3.85	2.55	1.96
SnCl ₆ ²⁻ + 18H ₂ O	4.72	3.11	2.38	3.13	2.06	1.58
SnCl ₅ (H ₂ O) ⁻ + 18H ₂ O	5.29	3.50	2.68	3.49	2.30	1.76
<i>cis</i> -SnCl ₄ (H ₂ O) ₂ + 18H ₂ O	6.02	4.00	3.07	4.00	2.66	2.04
<i>trans</i> -SnCl ₄ (H ₂ O) ₂ + 18H ₂ O	6.01	3.99	3.06	4.05	2.69	2.06

2.48 Å (equatorial and axial), 2.46 Å (equatorial) / 2.44 Å (axial), and 2.45 Å, respectively. The average Sn-Cl bond length of SnCl₆²⁻ agrees with the EXAFS result (2.39 Å) by Sherman et al. (2000) within 0.1 Å. The average Sn-O bond lengths of SnCl₅(H₂O)⁻, *cis*- and *trans*-SnCl₄(H₂O)₂

are 2.22 Å, 2.18 Å, and 2.18 Å, respectively. Snapshots of these complexes at 330 K are shown in Fig. 5.

The FPMD simulations for vapor phase show that SnCl₄, SnCl₄(H₂O) and *trans*-SnCl₄(H₂O)₂ remained stable for over 25.0 ps at both 300 K and 368 K, whereas *cis*-

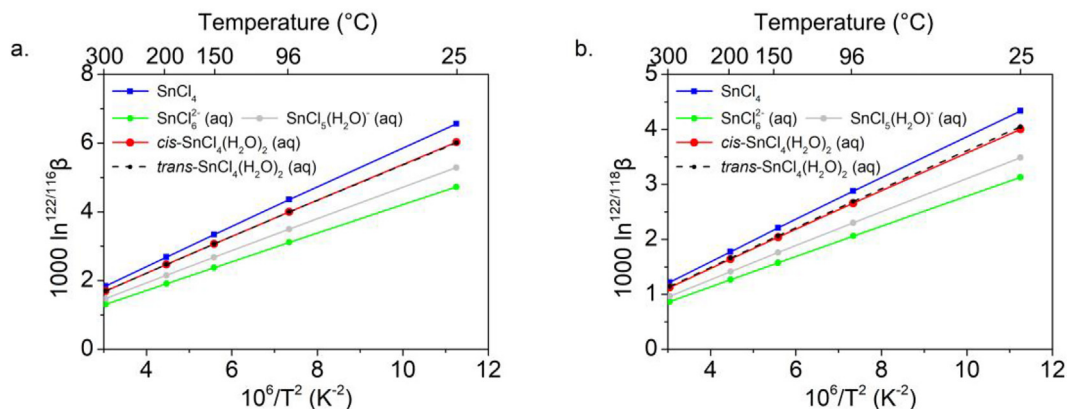


Fig. 7. Calculated $1000 \ln^{122/116} \beta$ (a) and $1000 \ln^{122/118} \beta$ (b) values for possible species of Sn in aqueous solution and vapor.

$\text{SnCl}_4(\text{H}_2\text{O})_2$ lost the one H_2O ligand spontaneously (Fig. 6a, b). In vapor phase at 300 K, the average Sn—Cl bond lengths of SnCl_4 , $\text{SnCl}_4(\text{H}_2\text{O})$ and $\text{trans-SnCl}_4(\text{H}_2\text{O})_2$ are 2.33 Å, 2.37 Å (equatorial)/2.36 Å (axial), and 2.43 Å, respectively; the average Sn—O bond lengths of $\text{SnCl}_4(\text{H}_2\text{O})$ and $\text{trans-SnCl}_4(\text{H}_2\text{O})_2$ are 2.61 Å and 2.38 Å, respectively.

4.3.2. Static quantum mechanical calculations

The optimized structures of gaseous $\text{Sn}^{4+}-\text{Cl}^-$ species are shown in Fig. S3. The calculated bond length and vibrational frequencies of SnCl_4 are listed in Table 3 for comparison with previous calculation results and experimental measurements. SnCl_4 has a Sn—Cl bond length of 2.31 Å, consistent with previous *ab initio* and experimental studies (Table 3). The vibrational frequencies of the isotopomers are provided as supplementary information. Overall, these comparisons show that the computational setup reasonably reproduces the structures and vibrations of $\text{Sn}^{4+}-\text{Cl}^-$ complexes.

The Gibbs free energy changes (ΔG) of the dehydration processes of $\text{SnCl}_4(\text{H}_2\text{O})$ and $\text{cis-} / \text{trans-SnCl}_4(\text{H}_2\text{O})_2$ at ambient conditions, 368 K and 423 K are listed in Table 4. All these values are negative, indicating spontaneous dehydration for these reactions. This indicates that SnCl_4 is the dominant gaseous species whereas $\text{SnCl}_4(\text{H}_2\text{O})$ and $\text{cis-} / \text{trans-SnCl}_4(\text{H}_2\text{O})_2$ are unstable. Therefore, in the following Discussions section, we only discuss the Sn isotope fractionation between SnCl_4 and aqueous Sn(IV) chloride species.

The calculated $1000 \ln^{122/116} \beta$ and $1000 \ln^{122/118} \beta$ values of $\text{Sn}^{4+}-\text{Cl}^-$ species at 25, 96, and 150 °C are listed in Table 5. There is negligible Sn isotope fractionation between the two isomers of $\text{SnCl}_4(\text{H}_2\text{O})_2$. The enrichment of ^{122}Sn decreased in the order $\text{SnCl}_4 > \text{SnCl}_4(\text{H}_2\text{O}) > \text{cis-SnCl}_4(\text{H}_2\text{O})_2 \approx \text{trans-SnCl}_4(\text{H}_2\text{O})_2 > \text{SnCl}_5(\text{H}_2\text{O})^- > \text{SnCl}_6^{2-}$ (Fig. 7). The equilibrium isotope fractionation factor $\Delta_{\text{eq}}^{122/116} \beta$ between $\text{SnCl}_4(\text{g})$ and the aqueous Sn(IV) chloride species ranges from 0.35‰ to 1.24‰ at 96 °C, and from 0.27‰ to 0.96‰ at 150 °C. The $\Delta_{\text{eq}}^{122/118} \beta$ between $\text{SnCl}_4(\text{g})$ and the aqueous Sn(IV) chloride species ranges from 0.22‰ to 0.82‰ at 96 °C, and from 0.17‰ to 0.63‰ at 150 °C.

5. DISCUSSIONS

5.1. Sn isotope fractionation during evaporation

The loss of Sn during the evaporation experiments was due to the release of some Sn-bearing species into the air. The shift to higher $\delta^{122/116}\text{Sn}$ (or $\delta^{122/118}\text{Sn}$) values of the residue after evaporation, therefore, is best explained by Sn isotope fractionation during evaporation. Evaporation of liquids and silicate melts can be well described by the Rayleigh fractionation function (Davis et al., 1990; Deng et al., 2018; Richter et al., 2007). Because the solution was open to air during evaporation, Sn fractionation during the evaporation experiment likely also followed a Rayleigh fractionation function (Johnson et al., 2004; Rodríguez et al., 2018):

$$(1000 + \delta_f) / (1000 + \delta_i) = F^{(\alpha-1)} \quad (11)$$

where δ_i and δ_f are the $\delta^{122/116}\text{Sn}$ (or $\delta^{122/118}\text{Sn}$) values of the original Sn solution and the remaining Sn (with a fraction of F) in aqueous solution after evaporation, respectively. α is the instantaneous Sn fractionation factor (in either $^{122/116}\text{Sn}$ or $^{122/118}\text{Sn}$) between vapor and liquid phases. And the isotopic difference between the initial and remained Sn is defined as:

$$\Delta = \delta_f - \delta_i \quad (12)$$

Fig. 4a shows that the experimental data can be fitted using a simple Rayleigh fractionation model and a $^{122/116}\alpha$ of 0.99940–0.99975 (or 0.99962 to 0.99984 in $^{122/118}\alpha$). If we assume that all experiments were governed by the same Sn isotope fractionation mechanism and the scatter in data points represents experimental and analytical uncertainties, the Sn isotope fractionation factor could be obtained using a least-squares optimization approach. In light of this, Equation (11) is transformed to:

$$\ln((1000 + \delta_f) / (1000 + \delta_i)) = (\alpha - 1) \ln F \quad (13)$$

Equation (13) shows that Rayleigh processes result in linear trends in the space of $\ln((1000 + \delta_f) / (1000 + \delta_i))$ versus $\ln F$, with fractionation factor (α) as the slope of the linear trend. In this way, we derive a $^{122/116}\alpha$ of 0.999642 (or

Table 6
Summary of different Sn isotope fractionation mechanisms and the respective predicted isotope fractionation factors.

Model	$\Delta^{122/116}\text{Sn}$ (‰)	Match observation	
Equilibrium (96 °C)	$\text{SnCl}_4(\text{g}) - \text{SnCl}_6^{2-}(\text{aq.})$ 1.24	$\text{SnCl}_4(\text{g}) - \text{trans-SnCl}_4(\text{H}_2\text{O})_2(\text{aq.})$ 0.36	No
	$\text{SnCl}_4(\text{g}) - \text{SnCl}_6^{2-}(\text{aq.})$ 0.96	$\text{SnCl}_4(\text{g}) - \text{trans-SnCl}_4(\text{H}_2\text{O})_2(\text{aq.})$ 0.28	Yes Wang et al. (2019a)
Simple kinetic (ideal gas)	H_2SnCl_6 -8.95	HSnCl_5 -11.44	No
Collisional diffusion	H_2SnCl_6 -0.46	HSnCl_5 -0.74	No
	H_2SnCl_6 -0.23	$\text{SnCl}_4(\text{g})$ -0.37	Yes
Equilibrium (96 °C) and kinetic	$\text{SnCl}_4(\text{g}) - \text{SnCl}_6^{2-}(\text{aq.})$ 0.50	$\text{SnCl}_4(\text{g}) - \text{trans-SnCl}_4(\text{H}_2\text{O})_2(\text{aq.})$ -0.38	Yes

$^{122/118}\alpha$ of 0.999763) with a least-squares linear regression (Rodríguez et al., 2018) (Fig. 4a, b). This equals an apparent $\Delta^{122/116}\text{Sn}$ fractionation factor of -0.358‰ (or $\Delta^{122/118}\text{Sn}$ of -0.237‰ ; Fig. 4c, d) between the Sn in vapor and Sn in aqueous solution. Thus according to a Rayleigh model, a Sn isotope fractionation of -0.36‰ occurs during evaporation of SnCl_4 in HCl matrix solutions at 96 °C. Note that in Fig. 4 the experimental results of evaporation of SnCl_4 in 8 M HCl at 150 °C by Wang et al. (2019a) are also plotted.

5.2. Mechanism of Sn isotope fractionation during volatilization

5.2.1. Equilibrium Sn isotope fractionation between vapor and aqueous solution

Evaporation processes may involve equilibrium isotope fractionation for a variety of elements. For example, equilibrium isotope fractionation takes place between vapor and melt for cadmium (Wombacher et al., 2004) and zinc (Zhang and Liu, 2018). Although significant equilibrium Sn isotope fractionation is predicted between minerals of Sn(II) and Sn(IV) valence (Polyakov et al., 2005), equilibrium isotope fractionation associated with reduction of Sn (IV) does not apply to our experiment because Sn(IV) chloride was used as the starting material and evaporation was performed in oxygenated open air, where Sn(II) cannot be stable.

FPMD simulations and static quantum mechanical calculations show that SnCl_6^{2-} , $\text{SnCl}_5(\text{H}_2\text{O})^-$ and *cis-* / *trans-* $\text{SnCl}_4(\text{H}_2\text{O})_2$ are the stable species of Sn(IV) in aqueous solution and SnCl_4 is the dominant Sn(IV) species in vapor phase. Further, quantum mechanical calculation results show that under equilibrium, $\text{SnCl}_4(\text{g})$, the dominant Sn (IV) species in vapor, is enriched in heavy Sn isotopes relative to the Sn(IV) species in aqueous solutions (Fig. 7). The equilibrium isotope fractionation factors are temperature- and species- dependent, and at 96 °C, Sn isotope fractionation factors ($\Delta^{122/116}\text{Sn}$) between $\text{SnCl}_4(\text{g})$ and aqueous Sn (IV) species vary from 1.24‰ for aqueous SnCl_6^{2-} to 0.35‰ for aqueous *cis-* $\text{SnCl}_4(\text{H}_2\text{O})_2$. If equilibrium isotope fractionation of Sn occurs during evaporation of Sn(IV) chloride solution, the vapor phase would enrich heavy Sn isotopes by 0.35–1.24‰ in $^{122/116}\text{Sn}$ (or 0.19–0.82‰ in $^{122/118}\text{Sn}$), depending on the speciation of Sn in aqueous solution. However, the direction of Sn isotope fractionation observed from the evaporation experiments is opposite to this prediction. Thus, equilibrium isotope fractionation alone cannot explain our evaporation experiment results (Table 6).

5.2.2. Kinetic Sn isotope fractionation by diffusion: The simple and sophisticated models

In an ideal gas, different species have identical average kinetic energy ($E = (1/2) \times mv^2$), thus the gaseous atoms/molecules with lower mass would have higher average velocity, following a relation of $v \propto m^{-1/2}$ (White, 2013). This velocity difference between gaseous molecules of different isotopes can cause a difference in diffusion coefficients, leading to mass-dependent kinetic isotope fractionation

(McNaughton and Rosman, 1991). It has been proposed that kinetic isotope fractionation factors can be described using a function $\alpha_{ik} = (\gamma_i/\gamma_k) \cdot (m_k/m_i)^{1/2}$ (Richter et al., 2007; Estrade et al., 2009; Zhang et al., 2014; Zhang and Liu, 2018), where the evaporation coefficients (γ) are assumed to be identical for isotopologues of a given element. Additionally, ion desolvation processes are accompanied by kinetic isotope fractionation that can be mathematically described in a form similar to the diffusion of ideal gas (Hofmann et al., 2012).

If the loss of Sn chloride from aqueous solution is envisioned as a process of differential diffusion of a certain Sn species, we can calculate the isotope fractionation factor based on the simple kinetic theory. For the dominant vapor species of SnCl₄, we obtain a kinetic isotope fractionation factor ($\Delta^{122/116}\text{Sn}_{\text{kinetic}}$) of -11.44% . If we consider other possible charge-neutral aqueous species that might be able to escape from the aqueous solution, the calculated $\Delta^{122/116}\text{Sn}_{\text{kinetic}}$ factors are -10.06% , -8.95% , -10.04% , and -9.47% for SnCl₄·2H₂O, H₂SnCl₆, HSnCl₅, and HSnCl₅·H₂O, respectively (Table 6). These results deviate from the experimental results (i.e., $\Delta^{122/116}\text{Sn} \approx -0.36\%$) remarkably. Although the direction of these isotope fractionation factors is consistent with experimental results, the values based on simple diffusion of ideal gas are more than one order of magnitude higher than observation. The diffusion coefficients of gaseous molecules derived from molecular weights define the theoretical upper limits of kinetic isotope effects by diffusion (Richter et al., 2006; Horita et al., 2008), nonetheless, such a simple theory is insufficient to provide detailed constraints for the volatilization mechanisms for Sn chlorides at atomic scales.

The isotope fractionation behaviors of oxygen during evaporation of water have been investigated in detail, and the discrepancy in fractionation factors between experiments and calculated values based on the simple kinetic theory have long been recognized (Merlivat, 1978; Barkan and Luz, 2007; Luz et al., 2009). In order to address the discrepancy, a molecular collision theory was developed (White, 2013). This theory considers the fact that evaporation under the Earth's surface condition involves collision of vapor molecules with other gaseous molecules at the boundary/transition layer between the aqueous and vapor phases. The liquid molecules collide with each other and some randomly gain enough kinetic energy that facilitates the escape from the transition layer by overcoming intermolecular forces. Based on the kinetic theory of gas as ideal rigid elastic spherical molecules (Merlivat, 1978), the molecular diffusivity ratio can be calculated according to the following equation (Merlivat, 1978; Cappa et al., 2003; Horita et al., 2008; Luz et al., 2009):

$$\frac{D_L}{D_H} = \left(\frac{M_H(M_L + M_G)}{M_L(M_H + M_G)} \right)^{1/2} \left(\frac{\Gamma_H + \Gamma_G}{\Gamma_L + \Gamma_G} \right)^2 \quad (14)$$

where Γ is the diameter of the diffusing species; subscripts L and H denote light and heavy isotopomers; G refers to the bath gas which the species diffuses in and collides with (steam in our case); M is the molecular mass. In addition, it is reasonable to assume identical collision diameters for isotopomeric molecules (Cappa et al., 2003). In this case,

the simplified molecular diffusivity ratio will be proportional to the inverse of square roots of the reduced masses, $\frac{M_i \cdot M_G}{M_i + M_G}$ (i denotes either light or heavy isotope) (Bourg and Sposito, 2007; Zhang and Liu, 2018). Our quantum mechanical calculation results show that the evaporation product is SnCl₄. Accordingly, the Sn isotope fractionation factor for diffusion across the boundary layer between aqueous and vapor phases during evaporation is -0.74% in $\Delta^{122/116}\text{Sn}$ (or -0.49 in $\Delta^{122/118}\text{Sn}$) for SnCl₄ (Table 6). Compared with the simple diffusion model for ideal gas without collision, this value is significantly closer to the observed Sn isotope fractionation factor. However, the calculated fractionation factor is still large in magnitude relative to the observed fractionation factor.

5.2.3. Evaporation with backward reaction

Extensive experiments of water evaporation have shown that O and H isotope fractionation factors are strongly controlled by humidity (Stewart, 1975; Cappa et al., 2003; Gonfiantini et al., 2018) and aerodynamic conditions at the water-air interface (Cappa et al., 2003; Gonfiantini et al., 2018), and different models have been proposed to explain the observed phenomenon. The successful models including turbulent diffusion (Cappa et al., 2003; Barkan and Luz, 2007; Gonfiantini et al., 2018) and coupled evaporation and condensation (Gat, 1996; Gonfiantini et al., 2018). Both models emphasize molecular-level processes at the boundary/transition layer between water and air. Below we apply these models to understand the observed Sn isotope fractionation beyond the kinetic isotope effects.

Stewart (1975) suggested a turbulent diffusivity ratio in formulizing the kinetic isotope fractionation factor during evaporation, that

$$\alpha^* = \left[\frac{D_H}{D_L} \right]^n \quad (15)$$

where D is the diffusion coefficient and n is the turbulent factor (n = 0 for turbulent diffusion; n = 1 for molecular diffusion) (Cappa et al., 2003). Gonfiantini et al. (2018) summarized that previous isotope studies on water evaporation could be explained with different turbulent indexes. Large isotope effects of molecular diffusivities will be obtained if turbulence is minimized (Luz et al., 2009). For the SnCl₄ evaporation experiments in our study, the observed Sn isotope fractionation ($\Delta^{122/116}\text{Sn}$ of -0.36% , close to the derived value -0.37%) can be derived when we assume turbulent factor n = 0.5 in a molecular collision theme (Horita et al., 2008; Luz and Barkan, 2010) (Table 6). This indicates a moderate degree of gas flow turbulence during evaporation (Barkan and Luz, 2007). The turbulence index reflects the aerodynamic condition at the water-air interface that cannot be directly measured (Gonfiantini et al., 2018). Based on the consistency between the calculated Sn isotope fractionation factor based on a turbulent diffusion model and the experimental results, we generalized a conceptual model for the evaporation experiment in our study (Fig. 8a). Kinetic isotope fractionation occurs when the vapor diffuses away from the interface, meanwhile the turbulence at the interface causes backward reactions. Backward condensation may bring the gaseous

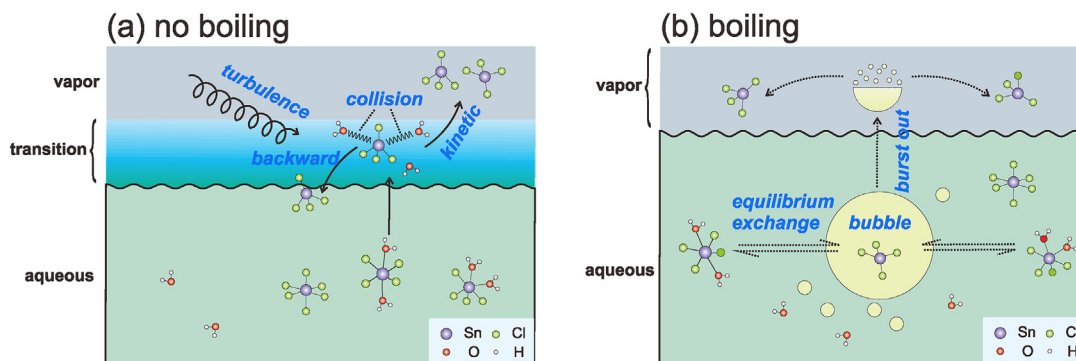


Fig. 8. Cartoon showing the conceptual model of Sn isotope fractionation during evaporation of Sn(IV) chloride solution at 96 °C (a); 150 °C (b).

species that contain lighter isotope back to the solution, as has been suggested in previous evaporation experiments (Craig et al., 1963; Yu et al., 2003).

It should be noted that the concurrence of outward and backward diffusion at the fluid-vapor interface facilitates exchange between the aqueous solution and vapor, which would lead to equilibrium isotope fractionation (Craig et al., 1963). In the models of coupled evaporation and condensation for describing fluxes and rates of evaporation, the observed isotope fractionation factor is the multiplication of equilibrium and kinetic fractionation factors (Richter et al., 2007; Estrade et al., 2009; Zhang et al., 2014; Zhang and Liu, 2018). According to Estrade et al. (2009), evaporation-condensation of mercury occur within a thin layer at liquid-vapor interface, where mercury atoms escape from or condense on. Balanced evaporation and condensation fluxes under chemical equilibrium conditions would lead to equilibrium isotope fractionation between liquid and vapor. Kinetic fractionation would emerge when evaporation outpaces condensation, and for water, the net isotope fractionation factor can be described (Cappa et al., 2003; Barkan and Luz, 2007; Luz et al., 2009) as: $\alpha_{\text{diff}} = (\alpha_{\text{evap}}/\alpha_{\text{eq}} - h)/(1 - h)$, where h represents the humidity in the environment and α_{evap} , α_{diff} , α_{eq} denote overall fractionation factor of evaporation, diffusion factor out of the transition interface (kinetic factor) and liquid-vapor equilibrium fractionation factor. For evaporation of substances other than water, h can be considered as zero, thus we have

$$\alpha_{\text{diff}} = \alpha_{\text{evap}}/\alpha_{\text{eq}} \quad (16)$$

Using the equilibrium fractionation factor derived from quantum mechanical calculations, and the kinetic isotope fractionation factor deduced from molecular collision theory (Section 4.2.2), an overall $\Delta^{122/116}\text{Sn}$ fractionation factor of 0.38‰ or 0.39‰ (for trans- or cis- $\text{SnCl}_4(\text{H}_2\text{O})_2$ in aqueous phase) is derived based on Eq. (14). This value also matches the experimental results well.

To summarize, either the collisional diffusion model (White, 2013) or the coupled evaporation and condensation model can be used to derive Sn isotope fractionation factors that matches experimental data. The two models deal with return of vapor species to aqueous solution in different mathematic forms, but in essence, they describe the fact

that backward reaction of evaporation occurs during evaporation, implying that kinetic isotope fractionation by collisional diffusion coupled with backward reaction at the fluids-vapor boundary caused the measured Sn isotope fractionation during evaporation experiments in this study.

5.2.4. Comparison with evaporation experiments at 150 °C

Evaporation experiment of Sn(IV) chloride solution at 150 °C was conducted by Wang et al. (2019a), who reported that isotopically heavy Sn was removed from the aqueous solution during evaporation. This direction of Sn isotope fractionation is consistent with our quantum mechanical calculations that gaseous SnCl_4 is isotopically heavier than other aqueous species of Sn(IV). Moreover, using a Rayleigh model (Fig. 4a), a Sn isotope fractionation factor ($\Delta^{122/116}\text{Sn}$) of 0.07–0.33‰ was derived from the results of Wang et al. (2019a), that is also consistent with the equilibrium isotope fractionation factors for Sn species at 150 °C (Table 6 and Table S4). Therefore, evaporation of SnCl_4 solution at 150 °C is likely accompanied with equilibrium Sn isotope fractionation.

The main differences in the Sn(IV) chloride evaporation experiments between this study and the study of Wang et al. (2019a) include the matrix of solution and temperature. The Sn(IV) chloride solution in Wang et al. (2019a) was in a matrix of 8 M HCl, whereas in this study, the Sn(IV) chloride was dissolved in 1 M to 4 M HCl. In this study, evaporation of Sn(IV) chloride in 1 M to 4 M HCl resulted in similar degree of Sn loss to vapor and consistent negative $\Delta^{122/116}\text{Sn}$ fractionation factor, implying that the molarity of HCl might not be the controlling factor of Sn isotope fractionation behavior. Temperature is also distinctly different between the two studies. It should be noted that in the Sn(IV) evaporation experiments by Wang et al. (2019a), the $\Delta^{122/116}\text{Sn}$ data with the lowest F factor is positive (first time series data in Fig. 4a), consistent with this study. This implies that during the heating stage of the evaporation experiment in Wang et al. (2019a), when temperature was likely lower than 150 °C, isotopically light Sn was indeed lost from aqueous solution. Therefore, difference in temperature of evaporation experiments is the most likely reason for the difference in Sn isotope fractionation behaviors between this study and the study of Wang et al. (2019a).

When temperature increases from 96 °C to 150 °C, boiling of the aqueous solution will take place, and bubbles form spontaneously within the liquid. This would produce saturation of vapor species in the bubbles and extensive backward reaction of evaporation at the bubble/fluid interface (Fig. 8b). This would facilitate adequate exchange between aqueous Sn and gaseous Sn, causing equilibrium Sn isotope fractionation between the aqueous and vapor phases. Indeed, evaporation experiments of water using bubbling dry air have shown to induce equilibrium O and H isotope fractionation (Gonfiantini et al., 2018).

5.3. Implications

The experiments in this study, together with the evaporation experiments by Wang et al. (2019a), show that significant Sn isotope fractionation can occur during drying of Sn chloride solutions, and the direction and magnitude of Sn isotope fractionation can vary depending on the evaporation conditions. This would result in analytical artifacts in Sn isotope analyses of natural samples. Therefore, in high precision Sn isotope studies, the effects of evaporation on Sn isotope fractionation during sample treatment must be taken into consideration. One should utilize double spike techniques to rigorously correct for possible Sn isotope fractionation (Creech et al., 2017; Wang et al., 2017) during evaporation, and the Sn double spike should be mixed with samples prior to digestion.

Tin mineralization can be related to transport of Sn as gaseous forms (Burt et al., 1982; Symonds et al., 1987; Hedenquist and Lowenstern, 1994; Williams-Jones and Heinrich, 2005; Chiaradia et al., 2018) although Sn in vapor phase does not always lead to economic mineralization as Sn partitions preferentially into the liquid phase in shallow settings (Heinrich et al., 1999). The volatile partitioning behavior of elements in hydrothermal processes depends on whether the process occurs in open or closed system (Drummond and Ohmoto, 1985), and the evaporation experiments in this study and that of Wang et al. (2019a) imply that the Sn isotope fractionation behaviors may be different accordingly. Phase separation related to fluids exsolved from deep intrusions under high pressure conditions may be associated with equilibrium Sn isotope fractionation between vapor and aqueous fluid, whereas catastrophic phase separation triggered by transition from lithostatic to hydrostatic pressure conditions (Heinrich et al., 1992; Korges et al., 2018) is likely a non-equilibrium process that is associated with kinetic Sn isotope fractionation. The diversity of Sn mineralization pathways, as well as the difference in Sn isotope fractionation behavior between vapor and aqueous phases of Sn chlorides under different physico-chemical conditions, implies that natural Sn isotope variability could be caused by Sn isotope fractionation associated with vaporization of Sn chlorides, in addition to Sn redox reactions (Polyakov et al., 2005; Wang et al., 2019a). Although the magnitude of Sn isotope fractionation related to vaporization is small relative to redox processes, the isotope effects of vaporization can be enhanced by coupling with Rayleigh distillation.

Since Sn is an abundant element in bronze, Sn isotope ratios have the potential to trace the provenance of antiquities given the large Sn isotope variability in natural cassiterites (Budd et al., 1995; Hausteiner et al., 2010; Nickel et al., 2012). Further, Sn isotopes may be used to study the history of ancient metallurgy because during the melting and casting process of bronze, evaporation of volatile tin species may cause Sn isotope fractionation (Budd et al., 1995; Yamazaki et al., 2014; Zhang et al., 2015; Berger et al., 2018).

Furthermore, Sn is a moderately volatile element and its isotopes may be used to identify different mechanisms for volatile depletion and isotopic variability in extraterrestrial samples (Creech et al., 2017; Creech and Moynier, 2019; Wang et al., 2019b). A recent Sn isotope study on lunar rocks (Wang et al., 2019b) revealed that lunar basalts are enriched in light Sn isotopes relative to the bulk silicate Earth, opposite to K and Zn that show light isotope depletion in lunar basalts. However, the volatility of Sn lies between K and Zn. Wang et al. (2019b) proposed that the different isotope fractionation behaviors between Sn and K/Zn could stem from speciation of the metals in the liquid and vapor phases during liquid–vapor separation. Specifically, the interpretation of Sn isotope data of lunar basalt by Wang et al. (2019b) is based on an assumption that the vapor species of Sn in protolunar disk was SnO. However, such assumption could be a topic of debate. We note that Cl content the bulk silicate Moon is estimated to be 6–40 ppm (Sharp et al., 2010; Boyce et al., 2018), up to two orders of magnitude higher than that of Sn. On the other hand, Sn is known to have high affinity to Cl to form tin chloride, therefore, it appears possible that Sn occurred as SnCl₂ in the vapor phase in protolunar disk. If so, vaporization of tin chloride (Chou et al., 1975; Yamazaki et al., 2013) could be responsible for the observed Sn isotope signature in lunar samples. Therefore, we argue that a better understanding of the Sn evaporation behavior and its isotopic effects is crucial for interpretations of Sn isotope data from extraterrestrial samples, and our SnCl₄ evaporation experiments, although at a very different condition from that of the protolunar disk, provide a necessary and relevant starting point for such understanding. Additional work is needed to explore the species and determine the fractionation factors of Sn for understanding the Moon-forming processes.

6. CONCLUSIONS

Evaporation experiments showed that Sn(IV) chloride can be transported as gaseous species. The stability of gaseous species of Sn was investigated by quantum mechanical calculations, which indicated that SnCl₄ is the dominant gaseous species of Sn(IV).

Evaporation of Sn(IV) chloride solutions at 96 °C in open air at 1 atmospheric pressure is associated with Sn isotope fractionation of $\Delta^{122/116}\text{Sn}_{\text{vapor-solution}} = -0.36\text{‰}$ (or $\Delta^{122/118}\text{Sn}_{\text{vapor-solution}} = -0.24\text{‰}$). However, quantum mechanics calculations yield Sn isotope fractionation factors in an opposite direction, that gaseous species of Sn

(IV) chloride enrich heavy Sn isotopes relative to aqueous species of Sn(IV) chloride by 0.35‰–1.24‰ in $\delta^{122/116}\text{Sn}$ (or 0.82‰–0.19‰ in $\delta^{122/118}\text{Sn}$) under equilibrium. This indicates that the evaporation of Sn(IV) chloride in our experimental conditions was associated with kinetic, rather than equilibrium isotope fractionation of Sn. Further, in order to explain the observed Sn isotope fractionation factors, the kinetic evaporation process of SnCl_4 molecule must be associated with molecular collision at the fluid-vapor interface zone, coupled with backward reaction. Comparison of our work with the evaporation experiments by Wang et al. (2019a) show that the Sn isotope fractionation behavior can be different under different physico-chemical conditions, implying that Sn isotopes could be used to understand metal volatilization behaviors at molecular level.

Declaration of Competing Interest

The authors declare that they have no known competing financial interests or personal relationships that could have appeared to influence the work reported in this paper.

ACKNOWLEDGEMENTS

This study was supported by the National Natural Science Foundation of China (No. 41622301 to W.Li, and No. 41572027, 41872041 to X.L.). X.L. also acknowledges supports from National Key R&D Program of China (2018YFA0702700), Newton International Fellowship Program, and the State Key Laboratory for Mineral Deposits Research at Nanjing University. We acknowledge the High Performance Computing Center (HPCC) of Nanjing University for doing the numerical calculations in this paper on its blade cluster system. We also thank Tao Yang, Huanling Lei and Qian Liu for assistance in lab work. This manuscript benefited from constructive comments from three anonymous reviewers as well as editorial comments from Prof. F. Moynier.

APPENDIX A. SUPPLEMENTARY MATERIAL

Supplementary data to this article can be found online at <https://doi.org/10.1016/j.gca.2019.10.033>.

REFERENCES

- Abascal M. B., Blaesing M., Ninomiya Y. and Mueller M. (2016) Influence of steam, hydrogen chloride, and hydrogen sulfide on the release and condensation of cadmium in gasification. *Energy Fuels* **30**, 943–953.
- Anders E. and Ebihara M. (1982) Solar-system abundances of the elements. *Geochim. Cosmochim. Acta* **46**, 2363–2380.
- Badullovich N., Moynier F., Creech J., Teng F. Z. and Sossi P. A. (2017) Tin isotopic fractionation during igneous differentiation and Earth's mantle composition. *Geochem. Perspect. Lett.* **5**, 24–28.
- Barkan E. and Luz B. (2007) Diffusivity fractionations of $(\text{H}_2^{16}\text{O})/(\text{H}_2^{17}\text{O})$ and $(\text{H}_2^{16}\text{O})/(\text{H}_2^{18}\text{O})$ in air and their implications for isotope hydrology. *Rapid Commun. Mass Spectrom.* **21**, 2999–3005.
- Becke A. D. (1993) Density-functional thermochemistry. 3. the role of exact exchange. *J. Chem. Phys.* **98**, 5648–5652.
- Berger D., Figueiredo E., Bruegmann G. and Pernicka E. (2018) Tin isotope fractionation during experimental cassiterite smelting and its implication for tracing the tin sources of prehistoric metal artefacts. *J. Archaeol. Sci.* **92**, 73–86.
- Bigeleisen J. and Mayer M. G. (1947) Calculation of equilibrium constants for isotopic exchange reactions. *J. Chem. Phys.* **15**, 261–267.
- Blanchard M., Balan E. and Schauble E. A. (2017) Equilibrium fractionation of non-traditional isotopes: a molecular modeling perspective. *Non-Traditional Stable Isotopes* **82**, 27–63.
- Bourg I. C. and Sposito G. (2007) Molecular dynamics simulations of kinetic isotope fractionation during the diffusion of ionic species in liquid water. *Geochim. Cosmochim. Acta* **71**, 5583–5589.
- Boyce J. W., Kane S. A., McCubbin F. M., Barnes J. J., Bricker H. and Treiman A. H. (2018) Early loss, fractionation, and redistribution of chlorine in the Moon as revealed by the low-Ti lunar mare basalt suite. *Earth Planet. Sci. Lett.* **500**, 205–214.
- Brockway L. O. and Wall F. T. (1934) The electron diffraction investigation of some non-metallic halides. *J. Am. Chem. Soc.* **56**, 2373–2379.
- Brugger J., Liu W., Etschmann B., Mei Y., Sherman D. M. and Testemale D. (2016) A review of the coordination chemistry of hydrothermal systems, or do coordination changes make ore deposits?. *Chem. Geol.* **447** 219–253.
- Budd P., Haggerty R., Pollard A. M., Scaife B. and Thomas R. G. (1995) New heavy isotope studies in archaeology. *Isr. J. Chem.* **35**, 125–130.
- Burt D. M., Sheridan M. F., Bikun J. V. and Christiansen E. H. (1982) Topaz rhyolites - distribution, origin, and significance for exploration. *Econ. Geol.* **77**, 1818–1836.
- Cappa C. D., Hendricks M. B., DePaolo D. J. and Cohen R. C. (2003) Isotopic fractionation of water during evaporation. *J. Geophys. Res.-Atmos.* **108**, 4525.
- Chaplygin I. V., Lavrushin V. Y., Dubinina E. O., Bychkova Y. V., Inguaggiato S. and Yudovskaya M. A. (2016) Geochemistry of volcanic gas at the 2012–13 New Tolbachik eruption, Kamchatka. *J. Volcanol. Geoth. Res.* **323**, 186–193.
- Chen H., Meshik A. P., Pravdivtseva O. V., Day J. M. D. and Wang K. (2019) Potassium isotope fractionation during high-temperature evaporation determined from the Trinity nuclear test. *Chem. Geol.* **522**, 84–92.
- Chiaradia M., Pujol-Sola N., Farre-de-Pablo J., Aiuppa A., Paonita A., Rizzo A. L. and Brusca L. (2018) Geochemistry and isotope composition (Sr, Pb, $\delta^{66}\text{Zn}$) of Vulcano fumaroles (Aeolian Islands, Italy). *Chem. Geol.* **493**, 153–171.
- Chou C. L., Boynton W. V., Sundberg L. L. and Wasson J. T. (1975) Volatiles on the surface of Apollo 15 green glass and trace-element distributions among Apollo 15 soils. In *Proc. Lunar Sci. Conf. 6th*, pp. 1701–1727.
- Clark R. J. H. and Mitchell P. D. (1975) Vapor-phase raman intensity studies on group-iv tetrachlorides. *J. Chem. Soc.-Farad. Trans. II* **71**, 515–524.
- Clark R. J. H. and Rippon D. M. (1972) Vapor-phase raman spectra, raman band contour analyses, coriolis constants, and force constants of spherical-top molecules MX_4 (m = group iv element, x = F, Cl, Br, or I). *J. Mol. Spectrosc.* **44**, 479–503.
- Cloquet C., Carignan J., Libourel G., Sterckeman T. and Perdrix E. (2006) Tracing source pollution in soils using cadmium and lead isotopes. *Environ. Sci. Technol.* **40**, 2525–2530.
- Craig H., Gordon L. I. and Horibe Y. (1963) Isotopic exchange effects in the evaporation of water: I. Low-temperature experimental results. *J. Geophys. Res.* **68**, 5079–5087.
- Creech J. B. and Moynier F. (2019) Tin and zinc stable isotope characterisation of chondrites and implications for early Solar System evolution. *Chem. Geol.* **511**, 81–90.

- Creech J. B., Moynier F. and Badullovich N. (2017) Tin stable isotope analysis of geological materials by double-spike MC-ICPMS. *Chem. Geol.* **457**, 61–67.
- Davis A. M., Hashimoto A., Clayton R. N. and Mayeda T. K. (1990) Isotope mass fractionation during evaporation of Mg_2SiO_4 . *Nature* **347**, 655–658.
- Day J. M. D., Moynier F., Meshik A. P., Pradivtseva O. V. and Petit D. R. (2017) Evaporative fractionation of zinc during the first nuclear detonation. *Sci. Adv.* **3** e1602668.
- Delaeter J. R. and Jeffery P. M. (1967) Tin - its isotopic and elemental abundance. *Geochim. Cosmochim. Acta* **31**, 969–985.
- Delaeter J. R., McCulloch M. T. and Rosman K. J. R. (1974) Mass-spectrometric isotope-dilution analyses of tin in stony meteorites and standard rocks. *Earth Planet. Sci. Lett.* **22**, 226–232.
- Deng Y., Li Y. and Li L. (2018) Experimental investigation of nitrogen isotopic effects associated with ammonia degassing at 0–70 °C. *Geochim. Cosmochim. Acta* **226**, 182–191.
- Drummond S. E. and Ohmoto H. (1985) Chemical evolution and mineral deposition in boiling hydrothermal systems. *Econ. Geol.* **80**, 126–147.
- Du D.-H., Wang X.-L., Yang T., Chen X., Li J.-Y. and Li W. (2017) Origin of heavy Fe isotope compositions in high-silica igneous rocks: A rhyolite perspective. *Geochim. Cosmochim. Acta* **218**, 58–72.
- Estrade N., Carignan J., Sonke J. E. and Donard O. F. X. (2009) Mercury isotope fractionation during liquid-vapor evaporation experiments. *Geochim. Cosmochim. Acta* **73**, 2693–2711.
- Foresman J. B. and Frisch E. (2015) *Exploring chemistry with electronic structure methods*, Third ed. Gaussian, Inc..
- Frisch M. J., Trucks G. W., Schlegel H. B., Scuseria G. E., Robb M. A. and Cheeseman J. R., et al. (2013) *Gaussian 09, Revision D.01*. Gaussian, Inc., Wallingford CT.
- Fujii H. and Kimura M. (1970) Molecular structure of tin tetrachloride as determined by gas-electron diffraction. *Bull. Chem. Soc. Jpn.* **43**, 1933–1939.
- Gat J. R. (1996) Oxygen and hydrogen isotopes in the hydrologic cycle. *Annu. Rev. Earth Planet. Sci.* **24**, 225–262.
- Giggenbach W. F. and Matsuo S. (1991) Evaluation of results from 2nd and 3rd iavei field workshops on volcanic gases, MT USU, Japan, and White-Island, New-Zealand. *Appl. Geochem.* **6**, 125–141.
- Goedecker S., Teter M. and Hutter J. (1996) Separable dual-space Gaussian pseudopotentials. *Phys. Rev. B* **54**, 1703–1710.
- Gonfiantini R., Wassenaar L. I., Araguas-Araguas L. and Aggarwal P. K. (2018) A unified Craig-Gordon isotope model of stable hydrogen and oxygen isotope fractionation during fresh or saltwater evaporation. *Geochim. Cosmochim. Acta* **235**, 224–236.
- Hargittai M. (2000) Molecular structure of metal halides. *Chem. Rev.* **100**, 2233–2301.
- Haustein M., Gillis C. and Pernicka E. (2010) Tin isotopy-a new method for solving old questions. *Archaeometry* **52**, 816–832.
- Hedenquist J. W., Aoki M. and Shinohara H. (1994) Flux of volatiles and ore-forming metals from the magmatic-hydrothermal system of satsuma iwajima volcano. *Geology* **22**, 585–588.
- Hedenquist J. W. and Lowenstern J. B. (1994) The role of magmas in the formation of hydrothermal ore-deposits. *Nature* **370**, 519–527.
- Heinrich C. A. (1990) The chemistry of hydrothermal tin-(tungsten) ore deposition. *Econ. Geol. Bull. Soc. Econ. Geol.* **85**, 457–481.
- Heinrich C. A., Gunther D., Audetat A., Ulrich T. and Frischknecht R. (1999) Metal fractionation between magmatic brine and vapor, determined by microanalysis of fluid inclusions. *Geology* **27**, 755–758.
- Heinrich C. A., Ryan C. G., Mernagh T. P. and Eadington P. J. (1992) Segregation of ore metals between magmatic brine and vapor - a fluid inclusion study using pike microanalysis. *Econ. Geol. Bull. Soc. Econ. Geol.* **87**, 1566–1583.
- Hofmann A. E., Bourg I. C. and DePaolo D. J. (2012) Ion desolvation as a mechanism for kinetic isotope fractionation in aqueous systems. *PNAS* **109**, 18689–18694.
- Holland H. D. and Turekian K. K. (2003) *Treatise on geochemistry. Elsevier Sci.* **7**.
- Hoover W. G. (1985) Canonical dynamics - equilibrium phase-space distributions. *Phys. Rev. A* **31**, 1695–1697.
- Horita J., Rozanski K. and Cohen S. (2008) Isotope effects in the evaporation of water: a status report of the Craig-Gordon model. *Isot. Environ. Health Stud.* **44**, 23–49.
- Johnson C. M., Beard B. L. and Albarède F. (2004) Overview and general concepts. *Rev. Mineral. Geochem.* **55**, 1–24.
- Kalugina Y. N. and Thakkar A. J. (2015) Electric properties of stannous and stannic halides: How good are the experimental values?. *Chem. Phys. Lett.* **626** 69–72.
- Koniger F. and Muller A. (1975) Combination of matrix-isolation and isotopic-substitution techniques - vibrational-spectra and molecular-constants of tin-tetrachloride. *J. Mol. Spectrosc.* **56**, 200–209.
- Korges M., Weis P., Lueders V. and Laurent O. (2018) Depressurization and boiling of a single magmatic fluid as a mechanism for tin-tungsten deposit formation. *Geology* **46**, 75–78.
- Lee C. T., Yang W. T. and Parr R. G. (1988) Development of the colle-salvetti correlation-energy formula into a functional of the electron-density. *Phys. Rev. B* **37**, 785–789.
- Li W., Jackson S. E., Pearson N. J., Alard O. and Chappell B. W. (2009) The Cu isotopic signature of granites from the Lachlan Fold Belt, SE Australia. *Chem. Geol.* **258**, 38–49.
- Lippert G., Hutter J. and Parrinello M. (1997) A hybrid Gaussian and plane wave density functional scheme. *Mol. Phys.* **92**, 477–487.
- Liu X., Lu X., Wang R. and Zhou H. (2012) Silver speciation in chloride-containing hydrothermal solutions from first principles molecular dynamics simulations. *Chem. Geol.* **294**, 103–112.
- Livingston R. L. and Rao C. N. R. (1959) Molecular structure of tin tetrachloride. *J. Chem. Phys.* **30**, 339–340.
- Lodders K. (2003) Solar system abundances and condensation temperatures of the elements. *Astrophys. J.* **591**, 1220–1247.
- Loss R. D., Rosman K. J. R. and Delaeter J. R. (1990) The isotopic composition of zinc, palladium, silver, cadmium, tin, and tellurium in acid-etched residues of the allende meteorite. *Geochim. Cosmochim. Acta* **54**, 3525–3536.
- Luz B. and Barkan E. (2010) Variations of O^{17}/O^{16} and O^{18}/O^{16} in meteoric waters. *Geochim. Cosmochim. Acta* **74**, 6276–6286.
- Luz B., Barkan E., Yam R. and Shemesh A. (2009) Fractionation of oxygen and hydrogen isotopes in evaporating water. *Geochim. Cosmochim. Acta* **73**, 6697–6703.
- Malinovsky D., Moens L. and Vanhaecke F. (2009) Isotopic fractionation of Sn during methylation and demethylation reactions in aqueous solution. *Environ. Sci. Technol.* **43**, 4399–4404.
- Marechal C. N., Telouk P. and Albarede F. (1999) Precise analysis of copper and zinc isotopic compositions by plasma-source mass spectrometry. *Chem. Geol.* **156**, 251–273.
- Mathur R., Powell W., Mason A., Godfrey L., Yao J. and Baker M. E. (2017) Preparation and measurement of cassiterite for sn isotope analysis. *Geostand. Geoanal. Res.* **41**, 701–707.
- McNaughton N. J. and Rosman K. J. R. (1991) Tin isotope fractionation in terrestrial cassiterites. *Geochim. Cosmochim. Acta* **55**, 499–504.
- McQuarrie D. A. and Simon J. D. (1999) *Molecular thermodynamics*. University Science Books.

- Merlivat L. (1978) Molecular diffusivities of H_2^{16}O , HD^{16}O , and H_2^{18}O in gases. *J. Chem. Phys.* **69**, 2864–2871.
- Migdisov A. A., Bychkov A. Y., Williams-Jones A. E. and van Hinsberg V. J. (2014) A predictive model for the transport of copper by HCl-bearing water vapour in ore-forming magmatic-hydrothermal systems: Implications for copper porphyry ore formation. *Geochim. Cosmochim. Acta* **129**, 33–53.
- Moynier F., Koeberl C., Beck P., Jourdan F. and Telouk P. (2010) Isotopic fractionation of Cu in tektites. *Geochim. Cosmochim. Acta* **74**, 799–807.
- Navarro-Flores A., Martínez-Frias J., Font X. and Viladevall M. (2000) Modelling of modern mercury vapor transport in an ancient hydrothermal system: environmental and geochemical implications. *Appl. Geochem.* **15**, 281–294.
- Nickel D., Haustein M., Lampke T. and Pernicka E. (2012) Identification of forgeries by measuring tin isotopes in corroded bronze objects. *Archaeometry* **54**, 167–174.
- Nose S. (1984a) A molecular-dynamics method for simulations in the canonical ensemble. *Mol. Phys.* **52**, 255–268.
- Nose S. (1984b) A unified formulation of the constant temperature molecular-dynamics methods. *J. Chem. Phys.* **81**, 511–519.
- Pauling L. and Brockway L. O. (1935) The radial distribution method of interpretation of electron diffraction photographs of gas molecules. *J. Am. Chem. Soc.* **57**, 2684–2692.
- Perdew J. P., Burke K. and Ernzerhof M. (1996) Generalized gradient approximation made simple. *Phys. Rev. Lett.* **77**, 3865–3868.
- Perrin D. D. (1982) *Ionisation constants of inorganic acids and bases in aqueous solution*, Second ed. Pergamon Press.
- Pokrovski G. S., Borisova A. Y. and Bychkov A. Y. (2013) Speciation and transport of metals and metalloids in geological vapors. *Thermodyn. Geotherm. Fluids* **76**, 165–218.
- Polyakov V. B., Mineev S. D., Clayton R. N., Hu G. and Mineev K. S. (2005) Determination of tin equilibrium isotope fractionation factors from synchrotron radiation experiments. *Geochim. Cosmochim. Acta* **69**, 5531.
- Pringle E. A., Moynier F., Beck P., Paniello R. and Hezel D. C. (2017) The origin of volatile element depletion in early solar system material: Clues from Zn isotopes in chondrules. *Earth Planet. Sci. Lett.* **468**, 62–71.
- Richards J. P. (2011) Magmatic to hydrothermal metal fluxes in convergent and collided margins. *Ore Geol. Rev.* **40**, 1–26.
- Richter F. M., Davis A. M., Ebel D. S. and Hashimoto A. (2002) Elemental and isotopic fractionation of Type B calcium-, aluminum-rich inclusions: Experiments, theoretical considerations, and constraints on their thermal evolution. *Geochim. Cosmochim. Acta* **66**, 521–540.
- Richter F. M., Janney P. E., Mendybaev R. A., Davis A. M. and Wadhwa M. (2007) Elemental and isotopic fractionation of Type B CAI-like liquids by evaporation. *Geochim. Cosmochim. Acta* **71**, 5544–5564.
- Richter F. M., Mendybaev R. A., Christensen J. N., Hutcheon I. D., Williams R. W., Sturchio N. C. and Beloso A. D. (2006) Kinetic isotopic fractionation during diffusion of ionic species in water. *Geochim. Cosmochim. Acta* **70**, 277–289.
- Righter K., Pando K., Marin N., Ross D. K., Righter M., Danielson L., Lapen T. J. and Lee C. (2018) Volatile element signatures in the mantles of Earth, Moon, and Mars: Core formation fingerprints from Bi, Cd, In, and Sn. *Meteorit. Planet. Sci.* **53**, 284–305.
- Rodríguez A., van Bergen M. J. and Eggenkamp H. G. M. (2018) Experimental evaporation of hyperacid brines: Effects on chemical composition and chlorine isotope fractionation. *Geochim. Cosmochim. Acta* **222**, 467–484.
- Schauble E. A. (2004) Applying stable isotope fractionation theory to new systems. *Geochim. Non-Traditional Stable Isotopes* **55**, 65–111.
- Schmidt C. (2018) Formation of hydrothermal tin deposits: Raman spectroscopic evidence for an important role of aqueous Sn(IV) species. *Geochim. Cosmochim. Acta* **220**, 499–511.
- Schulze M., Ziegerick M., Horn I., Weyer S. and Vogt C. (2017) Determination of tin isotope ratios in cassiterite by femtosecond laser ablation multicollector inductively coupled plasma mass spectrometry. *Spectrochimica Acta Part B-Atomic Spectrosc.* **130**, 26–34.
- Sharp Z. D., Shearer C. K., McKeegan K. D., Barnes J. D. and Wang Y. Q. (2010) The chlorine isotope composition of the moon and implications for an anhydrous mantle. *Science* **329**, 1050.
- Sherman D. M., Ragnarsdottir K. V., Oelkers E. H. and Collins C. R. (2000) Speciation of tin (Sn^{2+} and Sn^{4+}) in aqueous Cl solutions from 25 °C to 350 °C: an in situ EXAFS study. *Chem. Geol.* **167**, 169–176.
- Sossi P. A., Moynier F. and van Zuilen K. (2018) Volatile loss following cooling and accretion of the Moon revealed by chromium isotopes. *PNAS* **115**, 10920–10925.
- Stewart M. K. (1975) Stable isotope fractionation due to evaporation and isotopic exchange of falling waterdrops: Applications to atmospheric processes and evaporation of lakes. *J. Geophys. Res.* **80**, 1133–1146.
- Sulpizi M. and Sprik M. (2008) Acidity constants from vertical energy gaps: density functional theory based molecular dynamics implementation. *PCCP* **10**, 5238–5249.
- Symonds R. B., Rose W. I., Reed M. H., Lichte F. E. and Finnegan D. L. (1987) Volatilization, transport and sublimation of metallic and nonmetallic elements in high-temperature gases at merapi-volcano, indonesia. *Geochim. Cosmochim. Acta* **51**, 2083–2101.
- Tchounwou P. B., Ayensu W. K., Ninashvili N. and Sutton D. (2003) Environmental exposure to mercury and its toxicopathologic implications for public health. *Environ. Toxicol.* **18**, 149–175.
- Thanthiriwatté K. S., Vasiliu M., Battey S. R., Lu Q., Peterson K. A., Andrews L. and Dixon D. A. (2015) Gas phase properties of MX_2 and MX_4 ($X = \text{F}, \text{Cl}$) for $M =$ group 4, group 14, Cerium, and Thorium. *J. Phys. Chem. A* **119**, 5790–5803.
- Ulrich T., Gunther D. and Heinrich C. A. (1999) Gold concentrations of magmatic brines and the metal budget of porphyry copper deposits. *Nature* **399**, 676–679.
- Urey H. C. (1947) The thermodynamic properties of isotopic substances. *J. Chem. Soc.*, 562–581.
- VandeVondele J. and Hutter J. (2007) Gaussian basis sets for accurate calculations on molecular systems in gas and condensed phases. *J. Chem. Phys.* **127** 114105.
- VandeVondele J., Krack M., Mohamed F., Parrinello M., Chassaing T. and Hutter J. (2005a) QUICKSTEP: Fast and accurate density functional calculations using a mixed Gaussian and plane waves approach. *Comput. Phys. Commun.* **167**, 103–128.
- VandeVondele J., Mohamed F., Krack M., Hutter J., Sprik M. and Parrinello M. (2005b) The influence of temperature and density functional models in ab initio molecular dynamics simulation of liquid water. *J. Chem. Phys.* **122** 014515.
- Wagner W., Cooper J. R., Dittmann A., Kijima J., Kretzschmar H. J., Kruse A., Mares R., Oguchi K., Sato H., Stocker I., Sifner O., Takaishi Y., Tanishita I., Trubenbach J. and Willkommen T. (2000) The IAPWS industrial formulation 1997 for the thermodynamic properties of water and steam. *J. Eng. Gas Turbines Power-Trans. Asme* **122**, 150–182.

- Wang D., Mathur R., Powell W., Godfrey L. and Zheng Y. (2019a) Experimental evidence for fractionation of tin chlorides by redox and vapor mechanisms. *Geochim. Cosmochim. Acta* **250**, 209–218.
- Wang K., Moynier F., Podosek F. A. and Foriel J. (2012) An iron isotope perspective on the origin of the nanophase metallic iron in lunar regolith. *Earth Planet. Sci. Lett.* **337**, 17–24.
- Wang X., Amet Q., Fitoussi C. and Bourdon B. (2018) Tin isotope fractionation during magmatic processes and the isotope composition of the bulk silicate Earth. *Geochim. Cosmochim. Acta* **228**, 320–335.
- Wang X., Fitoussi C., Bourdon B. and Amet Q. (2017) A new method of Sn purification and isotopic determination with a double-spike technique for geological and cosmochemical samples. *J. Anal. At. Spectrom.* **32**, 1009–1019.
- Wang X., Fitoussi C., Bourdon B., Fegley B. and Charnoz S. (2019b) Tin isotopes indicative of liquid–vapor equilibration and separation in the Moon-forming disk. *Nat. Geosci.* **12**, 707–711.
- Weigend F. and Ahlrichs R. (2005) Balanced basis sets of split valence, triple zeta valence and quadruple zeta valence quality for H to Rn: Design and assessment of accuracy. *PCCP* **7**, 3297–3305.
- White W. M. (2013) *Geochemistry*. John Wiley & Sons, Ltd..
- Williams-Jones A. E. and Heinrich C. A. (2005) 100th Anniversary special paper: Vapor transport of metals and the formation of magmatic-hydrothermal ore deposits. *Econ. Geol.* **100**, 1287–1312.
- Williams-Jones A. E., Migdisov A. A., Archibald S. M. and Xiao Z. F. (2002) *Vapor-transport of ore metals*. Geochemical Society Special Publication.
- Wombacher F., Rehkamper M. and Mezger K. (2004) Determination of the mass-dependence of cadmium isotope fractionation during evaporation. *Geochim. Cosmochim. Acta* **68**, 2349–2357.
- Wunder B., Meixner A., Romer R. L. and Jahn S. (2011) Li-isotope fractionation between silicates and fluids: Pressure dependence and influence of the bonding environment. *Eur. J. Mineral.* **23**, 333–342.
- Xiao Y. K., Li S. Z., Wei H. Z., Sun A. D., Liu W. G., Zhou W. J., Zhao Z. Q., Liu C. Q. and Swihart G. H. (2007) Boron isotopic fractionation during seawater evaporation. *Mar. Chem.* **103**, 382–392.
- Yamazaki E., Nakai S., Sahoo Y., Yokoyama T., Mifune H., Saito T., Chen J., Takagi N., Hokanishi N. and Yasuda A. (2014) Feasibility studies of Sn isotope composition for provenancing ancient bronzes. *J. Archaeol. Sci.* **52**, 458–467.
- Yamazaki E., Nakai S. I., Yokoyama T., Ishihara S. and Tang H. (2013) Tin isotope analysis of cassiterites from Southeastern and Eastern Asia. *Geochem. J.* **47**, 21–35.
- Yao J., Mathur R., Powell W., Lehmann B., Tornos F., Wilson M. and Ruiz J. (2018) Sn-isotope fractionation as a record of hydrothermal redox reactions. *Am. Mineral.* **103**, 1591–1598.
- Yi W., Halliday A. N., Lee D. C. and Christensen J. N. (1995) Indium and tin in basalts, sulfides, and the mantle. *Geochim. Cosmochim. Acta* **59**, 5081–5090.
- Yu Y., Hewins R. H., Alexander C. M. O. and Wang J. (2003) Experimental study of evaporation and isotopic mass fractionation of potassium in silicate melts. *Geochim. Cosmochim. Acta* **67**, 773–786.
- Zhang J., Huang S., Davis A. M., Dauphas N., Hashimoto A. and Jacobsen S. B. (2014) Calcium and titanium isotopic fractionations during evaporation. *Geochim. Cosmochim. Acta* **140**, 365–380.
- Zhang J. and Liu Y. (2018) Zinc isotope fractionation under vaporization processes and in aqueous solutions. *Acta Geochimica* **37**, 663–675.
- Zhang Y., Liu B., Su Z., Chen J., Li G. and Jiang T. (2015) Volatilization behavior of SnO₂ reduced under different CO₂ atmospheres at 975 °C–1100 °C. *Int. J. Miner. Process.* **144**, 33–39.

Associate editor: Frederic Moynier